Journal of Hazardous Materials 423 (2022) 126993

Contents lists available at ScienceDirect

Journal of Hazardous Materials

journal homepage: www.elsevier.com/locate/jhazmat

Activated multi-walled carbon nanotubes decorated with zero valent nickel nanoparticles for arsenic, cadmium and lead adsorption from wastewater in a batch and continuous flow modes

Titus Chinedu Egbosiuba [a,b,d], Michael Chika Egwunyenga [a,e], Jimoh Oladejo Tijani [c,d], Saheed Mustapha [c,d], Ambali Saka Abdulkareem [b,d], Abdulsalami Sanni Kovo [b,d], Vida Krikstolaityte [f], Andrei Veksha [f], Michal Wagner [f], Grzegorz Lisak [f,g,*]

[a] Department of Chemical Engineering, Chukwuemeka Odumegwu Ojukwu University, PMB 02, Uli, Anambra State, Nigeria
[b] Department of Chemical Engineering, Federal University of Technology, PMB 65, Minna, Niger State, Nigeria
[c] Department of Chemistry, Federal University of Technology, PMB 65, Minna, Niger State, Nigeria
[d] Nanotechnology Research Group, Africa Centre of Excellence for Mycotoxin and Food Safety, Federal University of Technology, PMB 65, Minna, Niger State, Nigeria
[e] Department of Chemical Engineering, Delta State Polytechnic, PMB 1030, Ogwashi-Uku, Delta State, Nigeria
[f] Residues and Resource Reclamation Centre, Nanyang Environment and Water Research Institute, Nanyang Technological University, 1 Cleantech Loop, Clean Tech One, 637141, Singapore
[g] School of Civil and Environmental Engineering, Nanyang Technological University, 50 Nanyang Avenue, 639798, Singapore

ARTICLE INFO

Editor: Dr. Rinklebe Jörg

Keywords:
Nickel nanoparticles
Multi-walled carbon nanotubes
Heavy metals
Adsorption
Arsenic
Cadmium
Lead

ABSTRACT

Nickel nanoparticles (NiNPs) supported on activated multi-walled carbon nanotubes (MWCNTs) were used as an adsorbent applied towards Pb(II), As(V) and Cd(II) remediation from industrial wastewater. The result revealed the hydrophilic surface of MWCNTs-KOH was enhanced with the incorporation of NiNPs enabling higher surface area, functional groups and pore distribution. Comparatively, the removal of Pb(II), As(V) and Cd(II) on the various adsorbents was reported as NiNPs (58.6 ± 4.1, 46.8 ± 3.7 and 40.5 ± 2.5%), MWCNTs-KOH (68.4 ± 5.0, 65.5 ± 4.2 and 50.7 ± 3.4%) and MWCNTs-KOH@NiNPs (91.2 ± 8.7, 88.5 ± 6.5 and 80.6 ± 5.8%). Using MWCNTs-KOH@NiNPs, the maximum adsorption capacities of 481.0, 440.9 and 415.8 mg/g were obtained for Pb(II), As(V) and Cd(II), respectively. The experimental data were best suited to the Langmuir isotherm and pseudo-second order kinetic model. The fitness of experimental data to the kinetic models in a fixed-bed showed better fitness to Thomas model. The mechanism of metal ion adsorption onto MWCNTs-KOH@NiNPs show a proposed electrostatic attraction, surface adsorption, ion exchange, and pore diffusion due to the incorporated NiNPs. The nanocomposite was highly efficient for 8 adsorption cycles. The results of this study indicate that the synthesized nanocomposite is highly active with capacity for extended use in wastewater treatment.

1. Introduction

Water crisis emanating from the discharge of industrial effluents into the fresh water without treatment have continued to attract global attention and condemnation (Qu et al., 2020). This is because the wastewater contains heavy metals for instance lead (Pb), arsenic (As) and cadmium (Cd) that are non-biodegradable, highly mobile and ultimately toxic, causing severe threats to human health (Govarthanan et al., 2015; Ifthikar et al., 2020). For instance, As(V) is a known human carcinogen that is neurotoxic causing birth defects and damage to the liver and nervous system. Also, chronic exposure to Cd(II) is carcinogenic and cause serious damage to the lung, human bone, renal dysfunction and nervous system (Qu et al., 2020). Similarly, Pb(II) have been identified to cause cancer, anorexia plumbism, anemia, neuronal disorder and damage to the brain and kidney (Bhaumik et al., 2020). Thus, it is paramount to efficiently decontaminate wastewater of industrial origin from Pb(II), As(V) and Cd(II) before reuse or release into the natural water bodies, which can be validated by application of simple sensors (Ahamed et al., 2021; Ding et al., 2021, 2019; Ding and Lisak, 2019; Joon et al., 2020). For this purpose, World Health

* Corresponding author at: Residues and Resource Reclamation Centre, Nanyang Environment and Water Research Institute, Nanyang Technological University, 1 Cleantech Loop, Clean Tech One, 637141, Singapore.
E-mail address: g.lisak@ntu.edu.sg (G. Lisak).

https://doi.org/10.1016/j.jhazmat.2021.126993
Received 18 June 2021; Received in revised form 6 August 2021; Accepted 19 August 2021
Available online 25 August 2021

Organization (WHO) has suggested an overall permissible quantity of Pb (II), As(V) and Cd(II) for safe water to be 0.01, 0.01, and 0.003 mg/L (WHO, 2017).

Previously, numerous treatment procedures such as flocculation (Liu et al., 2021), reverse osmosis (Vaneeckhaute et al., 2019), chemical precipitation (Chen et al., 2018), phytoremediation (Cristaldi et al., 2017), ion exchange (Maslova et al., 2020), chemical oxidation (Yoo et al., 2017), ultrafiltration (Cao et al., 2020), membrane separation (Ibrahim et al., 2020), electro-dialysis (Min et al., 2021), bioremediation (Liu et al., 2018b), filtration (Azam et al., 2021), coagulation (Zhang et al., 2020c) and adsorption (Bhaumik et al., 2020) were applied to sequestrate Pb(II), As(V) and Cd(II) from industrial effluents. Moreover, a good number of the treatment methods were found complex, expensive and also produced toxic secondary pollutants (Govarthanan et al., 2018; Prakash et al., 2021; Zhao et al., 2020). Among others, adsorption had been ranked as the most promising and widely used treatment technique owing to its cost effectiveness, improvement in efficiency of removal and relatively ease operation (Saravanan et al., 2021). In this regard, a successful adsorption process depends apparently on the choice of a suitable sorbent with remarkable affinity to the target pollutants and a rapid rate of adsorption (Bhaumik et al., 2020).

Sequel to finding a suitable adsorbent for heavy metal elimination from industrial based effluents, nanomaterials have shown outstanding removal effectiveness in contrast to the conventional adsorbents ascribed to their high surface area associated with the availability of high amount of binding sites (Liu et al., 2020). Therefore, an increase in nanomaterials usage towards contaminants sequestration from wastewater has been observed in recent years (Ahmad et al., 2019). However, nanomaterials such as nanoparticles have been identified to exhibit the limitation such as difficulty in separation, aggregation leading to a pressure drop, especially in fixed-bed systems (Bhaumik et al., 2020). Recently, incorporation of nanoparticles into a porous matrix to produce an efficiently dispersed nanocomposite has been reported as the solution to the nanoparticle aggregation (Zhang et al., 2021a). Magnetic nanoparticles have been widely explored owing to their simplicity in separation. Among the magnetic nanoparticles, iron, copper, zinc, silver, titanium and gold have been mostly investigated (Almomani et al., 2020; Bounab et al., 2021; Doan et al., 2020; Gu et al., 2020; Naseem and Durrani, 2021; Prayoonpunratn et al., 2020). Unlike the frequently used metallic nanoparticles, studies on other nanoparticles such as nickel and their composites for heavy metals removal from industrial wastewater are inadequately addressed.

Carbon materials such as carbon nanotubes (CNTs) have been identified as a suitable support in the fabrication of nanocomposites with metallic nanoparticles owing to their large surface area, small size, porous tubular structural network, chemical, mechanical and thermal properties (Gödde et al., 2021; Zhao et al., 2021). Up to date, CNTs have been prepared from various materials including plastic wastes, carbonaceous, organic and inorganic materials using various pyrolytic processes such as arc-discharge (Yatom et al., 2017), laser ablation (Yang et al., 2019) and catalytic chemical vapor deposition (CCVD) (Chen et al., 2020). Although CNTs can be produced from various materials, their thermal properties, chemical properties, surface properties, mechanical properties and electrical properties are closely related (Bankole et al., 2018; Chen et al., 2020; Egbosiuba et al., 2020; Moo et al., 2019; Veksha et al., 2020). To reduce the hydrophobic properties of CNTs and increase the number of functional groups on the active sites of CNTs, it is important to functionalize them with heteroatoms prior to metallic particle deposition. Typically, the commonly used functional groups contain oxygen, nitrogen and sulfur, and enhance the anchoring of metallic nanoparticles. Previously, Winiarski et al. (2020) have reported the synthesis of multi-walled CNTs/nickel hydroxide composite and used as an electrochemical sensor for folic acid in food samples. Also, Gödde et al. (2021) reported the fabrication of nickel nanoparticles (NiNPs) onto nitrogen–doped CNTs as a CO_2 methanation catalyst which was stable, selective and very active. Recently, graphene oxide-carbon nanotube decorated NiNP nanocomposite was reported with excellent efficiency for Rhodamine B elimination from a liquid solution by adsorption (Hu et al., 2021). Similarly, Jin et al. (2018) the encapsulation of NiNPs in porous CNTs for highly efficient adsorption of dyes was reported. Zhang et al. (2021a) reported nitrogen doping in NiNP-embedded CNTs to enhance the overall oxidation of urea. Above all, the surface modification of multi-walled carbon nanotubes (MWCNTs) as functional material with NiNPs enhances the hydrophilicity of the nanocomposites surface towards the adsorption of heavy metals from wastewater.

The activation of MWCNTs surface with potassium hydroxide was followed by the synthesis and incorporation of NiNPs into the activated surface of MWCNTs-KOH producing a well dispersed nanocomposite (MWCNTs-KOH@NiNPs). The adsorption efficiencies of NiNPs, MWCNTs-KOH and MWCNTs-KOH@NiNPs were compared. MWCNTs-KOH@NiNPs having the highest adsorption efficiency were further applied in batch and fixed-bed ion adsorption modes to remove Pb(II), As(V) and Cd(II) from industrial wastewater. The choice of the target pollutants was due to their wide application in the adjoining battery, electroplating, plastics, cosmetics and paint industries, and subsequent discharge as effluents. In batch adsorption, the impact of solution pH, dosage, contact time, metal concentrations at initial values and temperature were investigated, while the fitting of the kinetic and isotherm data to the linear and nonlinear kinetic and isotherm models were compared. In addition, fixed-bed mode parameters of inlet metal concentration and flow rates as well as bed height were studied, while Yoon–Nelson, Thomas and Adams–Bohart models were considered in the continuous adsorption model. The reusability of MWCNTs-KOH@NiNPs was also investigated, while the role of MWCNTs-KOH decorated with NiNPs in the adsorption process of toxic metal ions was discussed.

2. Materials and methods

2.1. Materials

Analytical grade chemicals were utilized in this research (purity ranging from 95% to 99.5%). Nickel salt ($Ni(NO_3)_2{\cdot}6H_2O$), potassium hydroxide (KOH), sodium hydroxide (NaOH) pellet, trioxonitrate(V) acid (HNO_3), tetraoxosulphate(VI) acid (H_2SO_4), lead, arsenic and cadmium metals were procured from Sigma-Aldrich, Lagos. The chemicals did not undergo further purification prior to the application. In this research, Milli-Q system provided the deionized water for this study. The multi-walled carbon nanotubes (MWCNTs) utilized in this research were produced as reported elsewhere (Egbosiuba et al., 2020, 2021b) and briefly described in Section S.1 of the Supplementary information.

2.2. Synthesis of nickel nanoparticles

The preparation of extract from *Pterocarpus mildraedii* (PM) leaves was carried out by washing the leaves with deionized water prior to cutting of 50 g of the leaves into small sizes. Thereafter, the PM leaves were added in a conical flask containing deionized water (500 mL) and boiled for 20 min at 80 °C using a magnetic stirrer. At the end, the aqueous extract was subjected to solid particle removal by filtration with filter paper (Whatman No. 1). Thereafter, filtrate was stored at ambient temperature waiting for further application. Particularly in this synthesis, 90 mL of $Ni(NO_3)_2{\cdot}6H_2O$ (0.1 M) was poured into a conical flask prior to placement on a magnetic stirrer. Afterwards, 10 mL of PM aqueous extract (1 mg/mL) was poured into the nickel nitrate in the conical flask. Specifically, the mixtures were maintained at a constant pH (8) and stirred (300 rpm) continuously for 2 h at room temperature. The color change from light green to brown depicted the reduction of nickel ions (Ni^{2+}) to nickel (Ni^0) nanoparticles. Then again, UV–visible spectroscopy was applied for the confirmation of NiNPs formation. Subsequently, the obtained NiNPs were dried at 110 °C for the duration

of for 12 h prior to calcination at 500 °C for 6 h. After the calcination process, the dark green colored NiNPs were processed to a fine and uniform powder applying a mortar and a pestle. Finally, NiNPs were safely kept in an airtight container for further studies and their application.

2.3. Fabrication of MWCNTs-KOH@NiNPs

MWCNTs-KOH@NiNPs were synthesized by deposition/immobilization of NiNPs onto the surface matrix of MWCNTs-KOH. In the first place, the surface of MWCNTs was activated with 1 M KOH and 1 M HNO_3 prior to sonication using an ultrasonication bath (SB25-12DT, Ultrasonic Scientz) at 40 °C for the duration of 3 h. Thereafter, the obtained mixture was subjected to washing with distilled water to obtain pH 7, prior to drying in an oven for 12 h at 110 °C. The prepared MWCNTs-KOH were stored safely in a labeled airtight container and stored for future use. Further synthesis of MWCNTs-KOH@NiNPs was conducted by dispersing MWCNTs-KOH (0.5 g) in 50 mL of ethylene glycol (EG) through continuous sonication at 40 °C. Also, 0.5 g of NiNPs was added to the dispersed MWCNTs-KOH with continuous sonication to achieve homogeneity. Thereafter, the MWCNTs-KOH@NiNPs composite was oven dried at 110 °C for the duration of 12 h followed by calcination at 400 °C for 3 h. Subsequently, the nanocomposite was crushed to fine powder using a mortar and a pestle. The sample was stored in a well-labeled airtight container awaiting additional analysis and adsorption investigation.

2.4. Material characterization

In order to assess the morphology and microstructure of the nanomaterials, the NiNPs, MWCNTs-KOH and MWCNTs-KOH@NiNPs were subjected to high resolution scanning electron microscopy (HRSEM) and high resolution transmission electron microscopy (HRTEM) using Zeiss Auriga (UK) facility. The X-ray powder diffraction (XRD, 6000, Shimadzu Scientific) patterns were analyzed to determine the phase structures and crystalline behaviors of NiNPs, MWCNTs-KOH and MWCNTs-KOH@NiNPs. The nanomaterial chemical (structural) properties were explored using Fourier transform infrared spectroscopy (FTIR) spectra obtained using Frontier FTIR, PerkinElmer (UK). Thermogravimetric analysis (TGA, PerkinElmer, UK) with the attached derivative thermogravimetry (DTA) was used to determine the thermal stability of MWCNTs-KOH@NiNPs. The porous characteristics of NiNPs, MWCNTs-KOH and MWCNTs-KOH@NiNPs were characterized and calculated using the Brunauer–Emmett–Teller (BET, NOVA 4200, UK) model. The exploration of the adsorbent (MWCNTs-KOH@NiNPs) point of zero charge (PZC) was achieved implementing titration-based technique, whereby 0.05 g of the material (MWCNTs-KOH@NiNPs) was mixed with deionized water and surface charge on the adsorbent was adjusted using H_2SO_4 and NaOH in the range of pH 1–9 prior to the achievement of charge density of zero. Additionally, the detail for the reusability investigation of MWCNTs-KOH@NiNPs towards Pb(II), As (V) and Cd(II) removal are shown in Section S.4 of the Supplementary information.

2.5. Analysis of investigated metal ions

The chemical industrial wastewater was obtained from Nnewi (industrial area), located in Anambra Nigeria. The Pb(II), As(V) and Cd(II) in the obtained wastewater were assessed with atomic adsorption spectrometry (AAS, PG 990, PG Instruments, UK) and were subsequently identified as 92, 85, and 44 mg/L, respectively. The nickel concentration in the sampled wastewater was 2.5 mg/L. For adsorption tests, the various initial metal concentrations of 20, 60 and 100 mg/L were adjusted using the metal solutions. The supernatants were prepared using water bath (SB25-12DT, Scientz) followed by filtration and subsequent concentrations assessment of Pb(II), As(V) and Cd(II) using AAS technique.

2.6. Batch-based ion adsorption mode

In order to initially evaluate the equilibrium-based batch adsorption tests, the effect of different pHs, adsorbent dosages, contact times, initial metal concentrations and temperatures towards the efficient removal rates of Pb(II), As(V) and Cd(II) from the wastewater sample were conducted using a thermostatic water bath (SB25-12DT, Scientz). The parameter ranges were obtained from the literature sources and the appropriate conditions were then selected based on the preliminary tests. Also, the competitive adsorption performance was investigated by contacting various amounts (5, 10, 15, 20, 25 and 30 mg/L) of NiNPs, MWCNTs-KOH and MWCNTs-KOH@NiNPs adsorbents with 50 mL of 60 mg/L (Pb(II), As(V) and Cd(II)) in 100 mL vial and agitated (200 rpm) for 30 min at the temperature and pH (T = 303 K and pH = 5). The influence of solution pH (in the pH range of 2–6) was examined for removal of Pb(II), As(V) and Cd(II) using MWCNTs-KOH@NiNPs through adjusting the pH of the adsorbates at the various set values using 0.1 M H_2SO_4/NaOH at a constant assumed contact time (30 min), stirring speed of the solution (200 rpm), adsorbent dosage to the system (30 mg/L) and the applied temperature (303 K). The leaching ability of nickel in NiNPs was investigated after treatment of the wastewater sample at pH equal to 5.5, adsorbent dosage of the 30 mg/L, contact time of 60 min with the initial metal concentration of 60 mg/L.

To access the kinetic experimental data for ions such as Pb(II), As(V) and Cd(II) adsorption was recorded applying various intervals of contact times (10, 20, 30, 40, 60 and 120 min), 30 mg/L of MWCNTs-KOH@NiNPs was placed into 100 mL of wastewater and stirred solution with chosen speed of 200 rpm at a chosen constant and stable temperature and pH of 303 K and 5.5, respectively. Herein, the initial ions of interest concentrations of Pb(II), As(V) and Cd(II) ions were purposely varied at the range 20, 60 and 100 mg/L, respectively.

Further investigation of the equilibrium study was conducted using of MWCNTs-KOH@NiNPs (5, 10, 20, 30, 40 and 50 mg/L) at the chosen contact time (30 min), pH equal to 5.5, initial ion concentration of 100 mg/L and temperatures of 303, 313 and 323 K. Additionally, the influence of temperature on Pb(II), As(V) and Cd(II) adsorption capacity by MWCNTs-KOH@NiNPs was carried out at 303, 308, 313, 318, 323, 328, 333, 338 and 343 K using the following conditions: 40 mg/L adsorbent dosage, pH equal to 5.5 and the applied contact time of 30 min

At the end of the experimental study of the influence of pH, adsorbent dosage, contact time and temperature, 5 mL of the aliquot was withdrawn from the vial and filtered by grade 1 filter paper (Whatman). Thereafter, the analysis of the amount of all ions at equilibrium (C_e) was examined in the filtrate by AAS technique. To estimate uncertainty all tests were carried out multiple times (n = 3) with relative errors register to be less than 5%.

The adsorption process efficiency (reported as % removal) of ions at equilibrium and at any time was determined by employing Eqs. (1) and (2) (Bhaumik et al., 2020). Additionally, the capacity for investigated ions (Pb(II), As(V) and Cd(II)) adsorption by MWCNTs-KOH@NiNPs at equilibrium (q_e) was calculated by the application of Eq. (3) (Zhao et al., 2021), while the time-dependent Pb(II), As(V) and Cd(II) adsorption capacity (q_t) using MWCNTs-KOH@NiNPs was evaluated using Eq. (4) (Bhaumik et al., 2020).

$$\text{Removal efficiency}\ (\%) = \left(\frac{C_0 - C_e}{C_0}\right) \times 100 \tag{1}$$

$$\%\ \text{removal} = \left(\frac{C_0 - C_t}{C_0}\right) \times\ 100 \tag{2}$$

$$q_e = \left(\frac{C_0 - C_e}{m}\right) V \tag{3}$$

$$q_t = \left(\frac{C_0 - C_t}{m}\right)V \quad (4)$$

whereby, C_o (mg/L) relates to concentrations of Pb(II), As(V) and Cd(II) ions at initial conditions, while C_e and C_t (mg/L) illustrate the concentration at equilibrium conditions and at time (t). Also, *m* (mg) represents the adsorbent amount, while *V* (mL) refers to solution volume. In addition, the linear and nonlinear mathematical expressions for the isotherm and kinetic model are detailed in Sections S.2.1 and S.2.2, while the thermodynamic equations are described in S.2.3 of the Supplementary information.

2.7. Continuous-flow adsorption experiments

Continuous adsorption process of Pb(II), As(V) and Cd(II) was conducted using glass columns characterized with interior diameter and length of 2 and 30 cm, respectively, while the column volume was 500 mL at room temperature. The parameter values were selected based on the literature review and preliminary tests. The fixed-bed column was packed with 1, 1.5 and 2 g of MWCNTs-KOH@NiNPs to reach the specified adsorbent height equivalence of 2, 3 and 4 cm. The flow rates of ions, namely Pb(II), As(V) and Cd(II) solution through the column were 5, 6 and 7 mL/min, respectively. The concentrations of metal ions were 20, 60 and 100 mg/L, respectively, while pH of used solutions was constant at 5.5. Gauze and cotton wool were positioned at both bed ends to hinder flow channelization and enhance homogenous wastewater dispersion in the column. The metal solutions were circulated downwards in the column bed through the use of a peristaltic pump. The metal ion effluents were collected at specified intervals to assess the concentrations of Pb(II), As(V) and Cd(II) ions by AAS method.

To further validate the applicability of MWCNTs-KOH@NiNPs in the industry, effective prediction of the breakthrough curve from the continuous flow system was vital in establishing the design of facility, future operation and costs of maintenance (Ifthikar et al., 2020). The breakthrough curves denoted by the normalized concentration plot of the concentration of the effluent to the influent (C_t/C_o) against time. Meanwhile, the time for breakthrough (t_b) and time for exhaustion (t_e) were defined at C_t/C_o equivalence of 5% and 95%, respectively (Liu et al., 2019).

Total amounts of Pb(II), As(V) and Cd(II) ions adsorbed on a MWCNTs-KOH@NiNPs bed column at exhaustion point, q_{total} (mg) were evaluated using Eq. (5) (Albayati and Kalash, 2020; Ifthikar et al., 2020).

$$q_{total} = \frac{Q}{1000}\int_{t=0}^{t=t_{total}} (C_o - C_t)dt = \frac{(C_0 - C_t) \times Q \times t_e}{1000} = (C_0 - C_t) \times V_e \quad (5)$$

in which, Q (mL/min) refers to the flow rate, while ($C_o - C_t$) (mg/L) indicates the quantities of adsorbed ions. Parameters t_e (min) and V_e (L) are the saturation time of the MWCNTs-KOH@NiNPs bed column and the total volume of effluent collected till the saturation point. Also, C_o (mg/L) and C_t (mg/L) refer to the initial used concentrations of Pb(II), As (V) and Cd(II) ions at influent and V_e, respectively.

The total content of Pb(II), As(V) and Cd(II) adsorbed at exhaustion point per unit dry weight of MWCNTs-KOH@NiNPs that was added to the fixed-bed column, q_{eq} (equilibrium adsorption capacity) was evaluated by Eq. (6) (Aichour et al., 2019; Ifthikar et al., 2020).

$$q_{eq} = \frac{q_{total}}{m} \quad (6)$$

where m (g) is a total weight of mass (on a dry basis) of MWCNTs-KOH@NiNPs packed inside the fixed-bed based column.

Total removal of investigated ions (RM%) at the column exhaustion point was evaluated by Eq. (7) (Aichour et al., 2019).

$$RM\% = \frac{q_{total}}{m_{total}} \times 100 \quad (7)$$

whereby m_{total} refers to the total amount of Pb(II), As(V) and Cd(II) (mg) supplied through a MWCNTs-KOH@NiNPs fixed-bed column till exhaustion point. m_{total} was estimated by Eq. (8) (Aichour et al., 2019; Ifthikar et al., 2020; Singh et al., 2012).

$$m_{total} = \frac{C_o Q t_{total}}{1000} = \frac{C_o \times Q \times t_e}{1000} = C_o \times V_e \quad (8)$$

The equilibrium based concentrations of investigated ions, Pb(II), As (V) and Cd(II) C_e (mg/L) were evaluated with Eq. (9).

$$C_e = \frac{1000(m_{total} - q_{total})}{Qt_{total}} \quad (9)$$

The solid (adsorbent) and liquid (adsorbate) interaction time was denoted using empty bed contact time (EBCT) (min) and evaluated by the expression between the volume of the packed bed, V (L) and the flow rate, Q (mL/min) shown in Eq. (10).

$$EBCT = \frac{V}{Q} \quad (10)$$

Total adsorption of ions, namely Pb(II), As(V) and Cd(II) applying a MWCNTs-KOH@NiNPs bed column at breakthrough point, q_{tb} (mg) was estimated by Eq. (11) (Ifthikar et al., 2020).

$$q_{tb} = \frac{(C_0 - C_t) \times t_b \times Q}{1000} = (C_0 - C_b) \times V_b \quad (11)$$

where V_b (L) refers to the total volume of treated Pb(II)/As(V)/Cd(II) solution collected until the breakthrough point, while C_b (mg/L) and t_b (min) represents the metal concentration of V_b and the time for the fixed-bed column to achieve the breakthrough point.

Accordingly, the total amount of adsorbed ions at the point of breakthrough using a unit dry weight of MWCNTs-KOH@NiNPs filled inside the bed column, q_b (mg/g) was determined by Eq. (12) (Ifthikar et al., 2020).

$$q_b = \frac{q_{tb}}{m} \quad (12)$$

The hydraulic rate of loading, *u* (cm/min) was determined using Eq. (13) (Ifthikar et al., 2020).

$$u = \frac{Q}{\pi r^2} \quad (13)$$

where πr^2 (m^2) is the cross-sectional area of a fixed-bed column.

Furthermore, the linear and nonlinear mathematical expressions for the continuous flow kinetic models are expressed in Section S.3.1 of the Supplementary information.

2.8. Statistical data evaluation

In view of validating and comparing the fitting accuracy of the data from experimentations to the isotherm and kinetic models, statistical parameters such as determination coefficient (R^2), the residual sum of squares (SSE) and the chi-square (χ^2) were evaluated using Eqs. (14)–(16) (Alkurdi et al., 2021; Guo and Wang, 2019; Wang and Guo, 2020).

$$R^2 = \frac{\sum (q_{mean} - q_{cal})^2}{\sum (q_{cal} - q_{mean})^2 + \sum (q_{cal} - q_{exp})^2} \quad (14)$$

$$SSE = \sum (q_{exp} - q_{cal})^2 \quad (15)$$

$$\chi^2 = \sum \frac{(q_{exp} - q_{cal})^2}{q_{cal}} \quad (16)$$

3. Results and discussion

3.1. Characterizations

A typical HRSEM image of NiNPs displayed in Fig. 1a reveals a cubic and spherical shape of NiNPs that are non-uniformly dispersed with agglomerated clusters. In Fig. 1b, the HRTEM image of NiNPs also showed well dispersed cubic and spherical NiNPs which corroborated with the HRSEM result. The particle size distribution (Fig. 1c) of NiNPs ranged from 2 to 32 nm, with an average particle size of 17 nm. The MWCNTs surface was activated with KOH, and the HRSEM in Fig. 1d showed the entangled tubular network with the flanges of the deposited potassium (K). Particularly in our previous study, the surface morphology of MWCNTs indicating the presence of only carbon and oxygen were shown by HRSEM and validated by the elemental presence in energy dispersive X-ray spectrometer (EDS) (Egbosiuba et al., 202a, b). The HRTEM display of the MWCNTs-KOH further demonstrated the activated surface of the CNTs with whitish deposits of potassium on the surface of the cylindrical nanotubes as presented in Fig. 1e. The evaluated particle size distribution of MWCNTs-KOH (Fig. 1f) indicated the range of particle sizes from 2 to 16 nm, with an average size of 9 nm.

A typical HRSEM image of MWCNTs-KOH@NiNPs in Fig. 1g disclosed a smooth surface of tubular network and entangled CNTs with the deposited spherical Ni nanoparticles and K. The observed presence of K

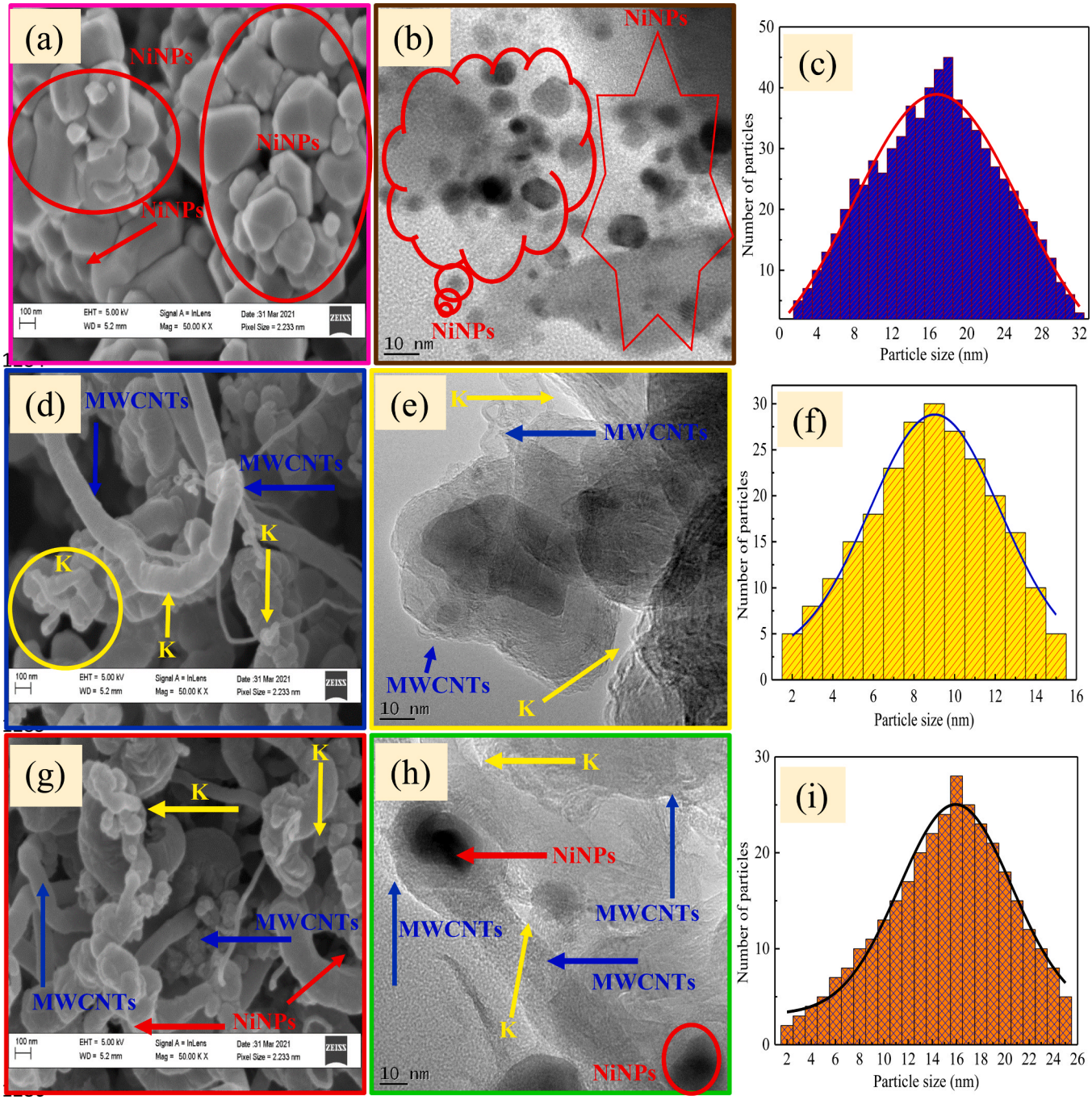

Fig. 1. (a) HRSEM image of NiNPs; (b) HRTEM image of NiNPs; (c) particle size distribution of NiNPs; (d) HRSEM image of MWCNTs-KOH; (e) HRTEM image of MWCNTs-KOH; (f) particle size distribution of MWCNTs-KOH; (g) HRSEM image of MWCNTs-KOH@NiNPs; (h) HRTEM image of MWCNTs-KOH@NiNPs and (i) particle size distribution of MWCNTs-KOH@NiNPs.

was highly negligible, which may be attributed to the extended washing process. Herein, the tube-like structures of MWCNTs-KOH@NiNPs were of different sizes and created an enabling avenue for rapid diffusion of metal ions. Apparently, the developed pores offer large surface area and adsorption sites for effective removal of heavy metal ions through possible diffusion to the available pores and subsequent attachment to the surface of the sorbent material (Zhang et al., 2020d). According to Fig. 1h, the HRTEM divulges the presence of K and the deposited Ni nanoparticles on the surface of curved network of tangled tubular structures that are closely contacted. As observed from the HRTEM, the lattice fringes characterized by 0.540 nm inter planar spacing on MWCNTs-KOH@NiNPs show resemblance to face centered cubic (fcc) crystal planes of Ni (111), revealing the high crystalline nature of the prepared NiNPs. However, Fig. 1i indicated that the particle size of MWCNTs-KOH@NiNPs increased from 2 to 26 nm, demonstrating an average of 14 nm. Overall, the elemental composition on the surface of MWCNTs-KOH@NiNPs were evaluated using EDS mapping procedure, which established peak correspondence to C, O, K and Ni elements as shown in Fig. S1a.

The structural crystallinity study of NiNPs, MWCNTs-KOH and MWCNTs-KOH@NiNPs was carried out by XRD and the result presented in Fig. 2a. According to Fig. 2a, metallic nickel was the predominant crystalline form of NiNPs, while graphite carbon was the main crystalline phase of MWCNTs. The XRD patterns of NiNPs displayed strong sharp diffraction peaks at 2 Theta values of 37.50°, 43.50°, 62.89°, 75.40° and 79.40°, which were allocated to (111), (200), (220), (311) and (222) crystal planes of (JCP2 cards No. 47-1049) (AlSalhi et al., 2020; Gödde et al., 2021; Zhang et al., 2021a). This implies that NiNPs were efficiently produced using PM extract. The occurrence of diffraction peaks on the activated surface of MWCNTs-KOH were discovered at 2θ of 26.27°, 45.40°, 52.89° and 77.60° which correspond to the crystal planes of graphite (002), (200), (102) and (311) (Egbosiuba et al., 2021b). However, Fig. 2a indicated that NiNPs reflections were detected on the surface of MWCNTs-KOH@NiNPs at 2θ values of the following crystal planes 37.50° (111), 43.50° (200), 62.89° (220), 75.40° (311) and 79.40° (222). In addition, the XRD patterns showed that the appearance of graphitic carbon was demonstrated on the MWCNTs-KOH@NiNPs through the peaks at 2θ of 26.27°, 50.87° and 77.60° assigned to the crystal planes (002), (102) and (311). The result revealed the possibility of a chemical interaction between the MWCNTs-KOH nanotubes and the deposited NiNPs due to the available functional groups. Furthermore, the crystallite sizes of the NiNPs, MWCNTs-KOH and MWCNTs-KOH@NiNPs were evaluated using Debye-Scherrer equation (Doan et al., 2020). The average crystallite sizes of 17.5, 8.9 and 14.2 nm were obtained for NiNPs, MWCNTs-KOH and MWCNTs-KOH@NiNPs, respectively.

The functional groups in the synthesized NiNPs and MWCNTs-KOH@NiNPs were investigated using FTIR spectra presented in Fig. 2b. Accordingly, FTIR of NiNPs showed major signals at 650, 875, 1430, 1628, 2324 and 3446 cm^{-1}, while the major bands on MWCNTs-KOH@NiNPs were identified at 650, 875, 1000, 1126, 1430, 1628, 2325 and 3446 cm^{-1}. Specifically, the bands present at 650 and 875 cm^{-1} were associated with possible bending vibrations of Ni—O—H bonds. The peak observed in Fig. 2b for MWCNTs-KOH@NiNPs at 1000 and 1126 cm^{-1} were assigned to the C—H and C—O stretch of phenolic group. Furthermore, the band observed at 1430, 1628 and 2324 cm^{-1} were ascribed to the presence of —OH, C=C as well as C=O bonds that are corresponding to the aromatic moieties, carbonyl groups, phenolic

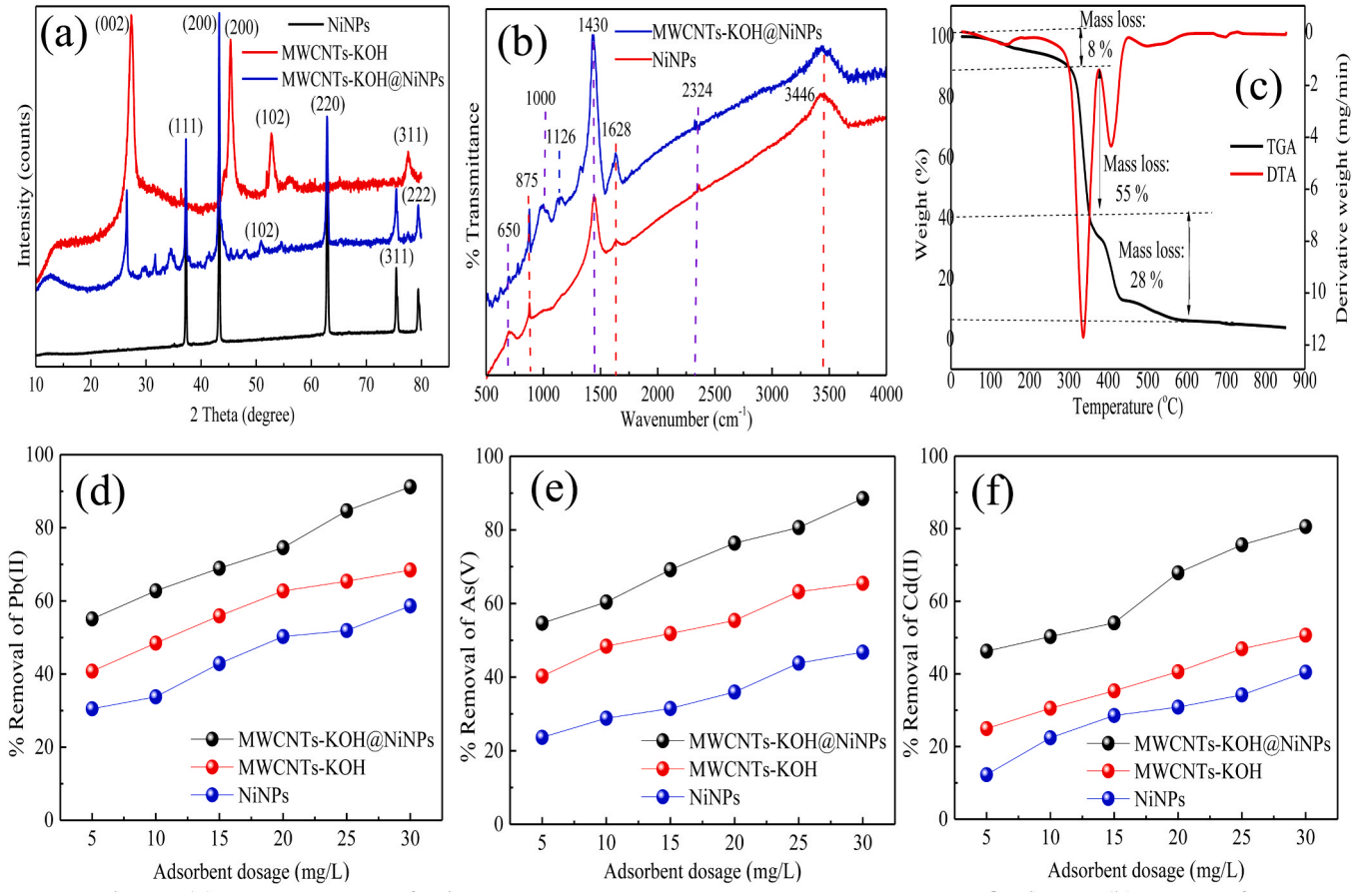

Fig. 2. (a) XRD pattern of NiNPs, MWCNTs-KOH and MWCNTs-KOH@NiNPs; (b) FTIR of NiNPs and MWCNTs-KOH@NiNPs; (c) TGA of MWCNTs-KOH@NiNPs: comparison of adsorption performance of (d) Pb(II); (e) As(V) and (f) Cd(II) using NiNPs, MWCNTs-KOH and MWCNTs-KOH@NiNPs at various doses (pH of 5, contact time of 30 min; initial concentration of 60 mg/L and temperature of 303 K).

and amino groups contained in the PM leaf extract (Doan et al., 2020). Particularly, the broad absorption identified at 3446 cm^{-1} were ascribed to the possible vibrational stretching of (—OH) functional groups of alcohol, carboxylic acids, carbohydrate and phenolic groups. Overall, the doping of MWCNTs-KOH with NiNPs was confirmed by the occurrence of peaks at 650, 875, 1000, 1126, 1430, 1628, 2324 and 3446 cm^{-1} in the FTIR spectrum of MWCNTs-KOH@NiNPs corresponding to Ni—O—H, C—H, C—O, C═C, C═O and —OH. Similar peaks were identified in the synthesis of NiNPs by Karpagavinayagam et al. (Karpagavinayagam et al., 2020) and in the composite of CNTs and NiNPs (Gödde et al., 2021; Hu et al., 2021; Zhang et al., 2021a).

To subsequently investigate the thermal stability of MWCNTs-KOH@NiNPs, thermogravimetric analysis (TGA) and derivative (DTA) weight loss were conducted as demonstrated in Fig. 2c. As can be seen from the result, three pronounced stages of weight loss were evident in the range of temperature 50–300 °C, 300–350 °C and 350–600 °C. The weight loss of 8% observed between 50 and 300 °C was associated with moisture loss in the adsorbent material. In the range of temperature 300–350 °C, rapid percentage weight loss of 55% was observed and attributable to the degradation of amorphous carbon in the adsorbent material. Further temperature increase from 350 to 500 °C resulted to a weight loss of 28% due to the volatilization and decarboxylation of functional moieties in the MWCNTs-KOH@NiNPs. Beyond the temperature, 600 °C insignificant weight loss occurred and may be linked to the degradation of the remaining small amount of organic and inorganic species in the MWCNTs-KOH@NiNPs composite. The obtained thermal profile in this study showed corresponding agreement with the literature (Bankole et al., 2018).

The measured surface area, total pore volume and pore size of NiNPs were 56 $m^2\ g^{-1}$, 0.045 $cm^3\ g^{-1}$ and 15 nm, respectively, while those of MWCNTs-KOH were 1230 $m^2\ g^{-1}$, 0.11 $cm^3\ g^{-1}$ and 24 nm. Additionally, the values of 1242 $m^2\ g^{-1}$, 0.12 $cm^3\ g^{-1}$ and 28 nm were obtained for the S_{BET}, pore volume and pore size of MWCNTs-KOH@NiNPs. The observed higher surface properties of MWCNTs-KOH@NiNPs over NiNPs and MWCNTs-KOH reveal the availability of greater interfacial area and binding sites for the occurrence of adsorbent-adsorbate interaction, thereby improving the removal efficiency of heavy metals from wastewater (Chowdhury et al., 2021). Notably, the obtained pore sizes for NiNPs, MWCNTs-KOH and MWCNTs-KOH@NiNPs fall within the range 2–50 nm demonstrating mesoporous characteristics of the prepared materials. In general, modifications in the surface properties of the MWCNTs-KOH decorated with NiNPs corroborated with the XRD patterns, FTIR spectrum, HRSEM and HRTEM images elucidating the incorporated NiNPs on the surface of MWCNTs-KOH.

3.2. Comparative adsorption performance of the adsorbents

Herein, NiNPs, MWCNTs-KOH and MWCNTs-KOH@NiNPs were applied to test and compare the adsorption process performance of investigated ions, Pb(II), As(V) and Cd(II). The result presented in Fig. 2 (d–f) revealed the adsorption efficiencies of the different adsorbents at various amounts of the adsorbent. According to Fig. 2(d–f), optimum adsorption of 91.2 ± 8.7% Pb(II), 88.5 ± 6.5% As(II) and 80.6 ± 5.8% Cd(II) was attained by MWCNTs-KOH@NiNPs, whereas Pb(II) (68.4 ± 5.0%), As(V)(65.5 ± 4.2%), Cd(II)(50.7 ± 3.4%) and Pb(II) (58.6 ± 4.1%), As(V)(46.8 ± 3.7%), Cd(II)(40.5 ± 2.5%) were achieved using MWCNTs-KOH and NiNPs, respectively. Based on the results, MWCNTs-KOH@NiNPs demonstrated better effectiveness towards Pb (II), As(V) and Cd(II) adsorption, compared to MWCNTs-KOH and NiNPs. The superior adsorption effectiveness of Pb(II), As(V) and Cd(II) using MWCNTs-KOH@NiNPs over MWCNTs-KOH and NiNPs may be associated with the increased hydrophilicity of the nanocomposites towards attraction of metal ions and the relatively higher surface area of developed nanocomposite. In addition, MWCNTs-KOH provided improved support for NiNPs during the fabrication of the nanocomposite, thence providing enhanced active sites for biding ions. Therefore, MWCNTs-KOH@NiNPs were further applied for the elimination of Pb(II), As(V) and Cd(II) from industry originated wastewater in batch and continuous flow adsorption modes.

3.3. Batch based ion adsorption

3.3.1. Effect of initial pH and ionic strength

Principally, solution pH plays a critical role towards the removal of heavy metals by modifying the functional group ionization degree, predominant metal ion speciation and sorbent surface charge (Rocha et al., 2016). In this study, MWCNTs-KOH@NiNPs were applied to remove Pb(II), As(V) and Cd(II) ions at metal initial concentration of 60 mg/L from wastewater with the pH of the solution ranging from 2–6. Initially, the pH of the solution was increased above pH 6 which enabled the formation and settlement of metal hydroxide precipitate at the solution bottom, thereby prompting the maintenance of pH in the range 2–6 (Ifthikar et al., 2020). The initial solution pH effect on the Pb(II), As (V) and Cd(II) uptake applying MWCNTs-KOH@NiNPs is demonstrated in Fig. 3a. In regards to Fig. 3a, metal ion adsorption capacity was low between pH 2–3, but increased to a maximum adsorption capacity of 255.5, 224.2 and 190.8 mg/g for Pb(II), As(V) and Cd(II) ions adsorption applying MWCNTs-KOH@NiNPs at the pH 5.5. Similarly, Fig. 3a also disclosed a relatively significant improvement in the efficiency of removal of the toxic heavy metals within the pH range of 4–5.5. Thence, the optimum removal efficiency of 99.9 ± 3.5, 96.3 ± 5.0 and 88.9 ± 4.5% was obtained for Pb(II), As(V) and Cd(II) uptake, respectively. Further increase in pH up to 6 did not translate to increasing removal of the metal ions, thus the experiment was stopped at pH 6 and precipitation at pH> 5.5 was not observed. Accordingly, pH 5.5 was the best pH for Pb(II), As(V) and Cd(II) adsorption applying MWCNTs-KOH@NiNPs and may be attributed to the relatively large amount of protonated adsorption sites that may participate in the adsorption of ions.

Further investigation of the adsorption behavior was performed using the zeta potential of MWCNTs-KOH@NiNPs at different pH (Fig. 3b). The MWCNTs-KOH@NiNPs point of zero charge (pH_{PZC}) was at 5.0. Meanwhile, the value of pH < pH_{PZC} indicated positive surface charge of the developed adsorbent attributed to the functional groups protonation and electrostatic repulsion of the sorbent positive charge surface and the adsorbate. However, the sorbent negative charge surface at pH > pH_{PZC} may be due to efficient deprotonation and increase in electrostatic interaction in the system of the negatively charged surface of the adsorbent with the positively charged ions, Pb(II), As(V) and Cd (II). (Bhaumik et al., 2020). Therefore, at the lower range of pH (pH < pH_{PZC} = 5.0) the reduction in the removal of ions by MWCNTs-KOH@NiNPs could be linked to the competitive interaction of protons (H^+) and individual studied ions as well as electrostatic repulsion of the positive surface charge of the adsorbent. At higher pH (pH > pH_{PZC} = 5.0), however, higher removal effectiveness for ions was favored which may be linked to electrostatic attraction of the adsorbent negative charge surface (deprotonated) and the cationic heavy metals. The results corroborated the remediation of water samples by removal of Pb(II), As(V) and Cd(II) applying MWCNTs-KOH@NiNPs was optimally attained at pH 5.5 and was utilized for further adsorption studies.

Generally, ionic strength is a significant parameter to determine the removal of heavy metals onto the adsorbent through specific and non-specific adsorption. In the specific adsorption, direct interactions/binding of the heavy metals onto the adsorbent applies and the removal of Pb(II)/As(V)/Cd(II) species may not change or increase with increasing ionic strength if the metal ion species form inner sphere surface complexes with the possibly present functional groups/moieties on the adsorbent surface (Wu et al., 2018). Conversely, the nonspecific heavy metal adsorption entails that the Pb(II)/As(V)/Cd(II) species decrease with increasing ionic strength attributable to outer sphere surface complexes formation by the metal ions through electrostatic attraction that influenced the adsorption of the retained hydration

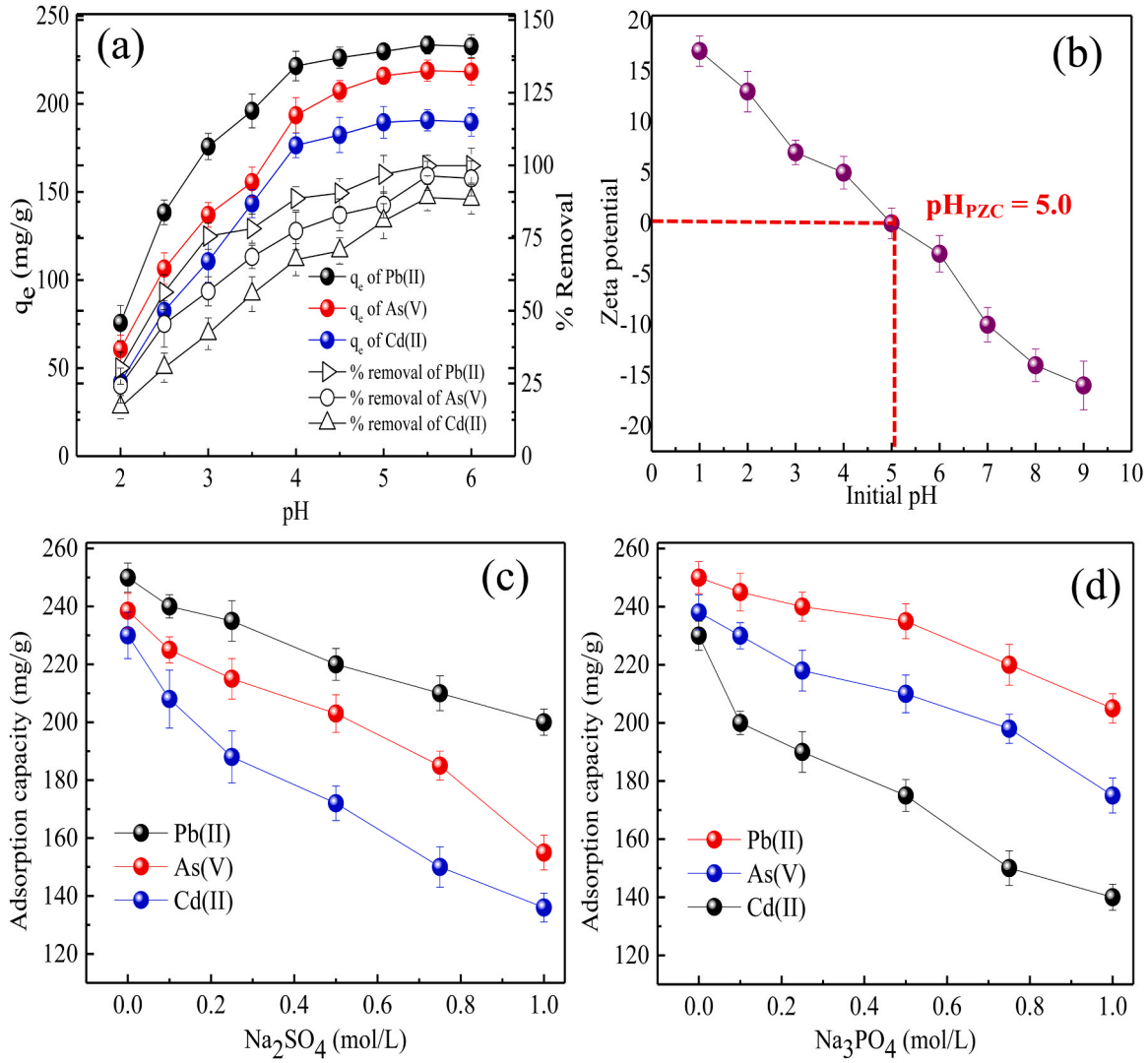

Fig. 3. (a) The pH effect on ion adsorption applying MWCNTs-KOH@NiNPs (initial concentration of metal ions of 60 mg/L, contact time of 30 min, adsorbent dosage of 30 mg/L and temperature of 303 K); (b) zeta potential of MWCNTs-KOH@NiNPs; effect of ionic strength on the adsorption of Pb(II), As(V) and Cd(II) by MWCNTs-KOH@NiNPs using (c) K_2SO_4 and (d) $Ca_3(PO_4)_2$ at the initial concentration of metal ions of 60 mg/L, pH equal to 5.5, contact time of 30 min, adsorbent dosage of 30 mg/L and temperature of 303 K.

sphere of the ions to the adsorbent (Lalhmunsiama et al., 2017). The specific adsorption process of heavy metals is basically not influenced by the solution ionic strength, while the nonspecific adsorption of metal ions is generally affected by changes in the solution ionic strength (Zhao et al., 2020). The effect of parameters of ionic strength on the adsorption capacity was studied at various concentrations of Na_2SO_4 and Na_3PO_4 to determine their impact on the surface charge of MWCNTs-KOH@NiNPs and the results shown in Fig. 3c and d. From Fig. 3c and d, clearly pointing that the adsorption of Pb(II), As(V) and Cd(II) using MWCNTs-KOH@NiNPs decreased with the increase in the concentrations of the competing ions. This may be due to the possible formation of moieties by Pb(II)/As(V)/Cd(II) and $Na^+/SO_4^{2-}/PO_4^{3-}$, which were attached to the surface of MWCNTs-KOH@NiNPs through outer sphere complexes. Additionally, competition of Pb(II)/As(V)/Cd(II) and the $Na^+/SO_4^{2-}/PO_4^{3-}$ may possibly decline the potential energy for the migration and heavy metals diffusion to the binding sites of the adsorbent at higher ionic strength, thereby influencing the adsorption capacity at equilibrium (Zhang et al., 2020d). The results obtained showed similarity to the reported trend over the literature (Lalhmunsiama et al., 2017; Wu et al., 2018). Furthermore, the concentration of nickel ion in the treated water was confirmed using AAS and the obtained value (0.03 mg/L) indicates efficient removal of nickel ion using MWCNTs-KOH@NiNPs. This result reveal that nickel present in the NiNPs did not leach into the treated water due to the calcination of NiNPa and MWCNTs-KOH@NiNPs at high temperature and the encapsulation of NiNPs onto the tubular network of MWCNTs.

3.3.2. *Kinetics consideration and effect related to the contact time*

The change in the sequestration of Pb(II), As(V) and Cd(II) applying MWCNTs-KOH@NiNPs in time domain was investigated at three various initial ion concentrations (Fig. 4a). As revealed by the results, the adsorption of ions (Pb(II), As(V) and Cd(II)) was rapid within the first 20 min, which can be linked at large to sites available for binding at the initial contact and the adsorption capacity of MWCNTs-KOH@NiNPs attained saturation at 60, 40 and 30 min, respectively for the metal ion initial concentrations of 20, 60 and 100 mg/L. The MWCNTs-KOH@NiNPs adsorption capacity for Pb(II), As(V) and Cd(II) at the saturation stage for different initial metal concentrations of 20, 60 and 100 mg/L were 128.4, 243.8 and 408.2 mg/g for Pb(II), 116.0, 220.88 and 374.3 mg/g for As(V) and 105.8, 201.8 and 327.5 mg/g for Cd(II), respectively. The rapid adsorption process of Pb(II), As(V) and Cd(II) onto MWCNTs-KOH@NiNPs may be ascribed to adsorption capacity

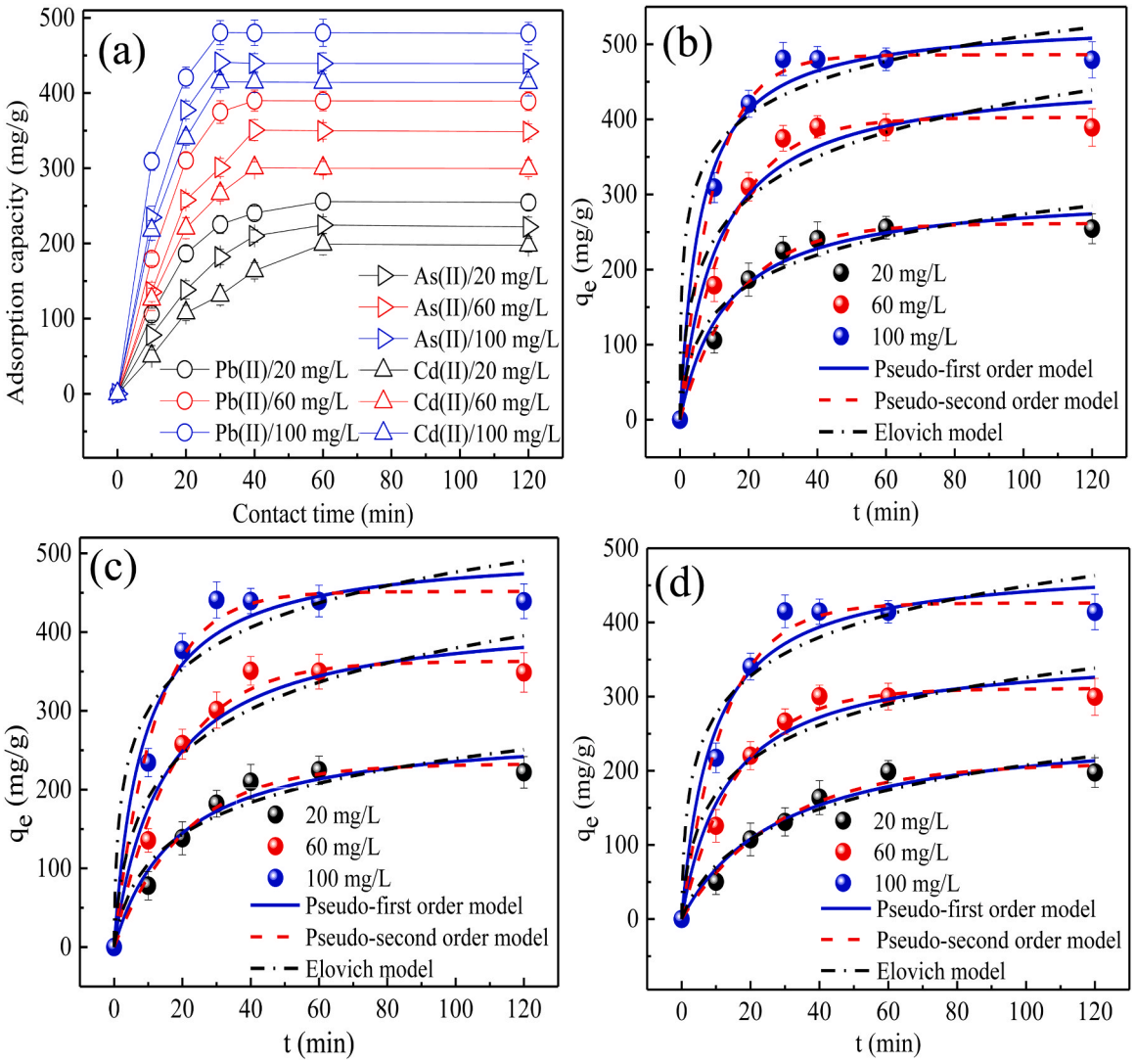

Fig. 4. (a) The contact time effect on the Pb(II), As(V) and Cd(II) adsorption at different initial metal concentrations applying MWCNTs-KOH@NiNPs; the kinetic data fitting of (b) Pb(II); (c) As(V) and (d) Cd(II) to nonlinear pseudo-first order, pseudo-second order and Elovich kinetic models (pH equal to 5.5, adsorbent dosage of 30 mg/L and temperature of 303 K).

increment due to the increase in the initial metal concentrations. However, further considering contact time beyond that corresponding to the equilibrium time led to insignificant removal of the metal ions which may be attributed to the availability of active adsorption sites (Zhao et al., 2020). Apparently, among the various reported contact times in the literature shown in Table 1, the adsorption of the heavy metals using different initial metal concentrations (20, 60 and 100 mg/L) achieved optimum adsorption capacity at a smaller contact time of 60, 40 and 30 min. The observed variations could be ascribed to the variations in the materials synthesis, surface properties, functional groups, morphological and structural arrangements with the MWCNTs-KOH@NiNPs.

Compared to As(V) and Cd(II), more of Pb(II) ions were adsorbed at various initial metal concentrations and may be owing to the variances in their ionic radius and degree of electronegativity (Kharrazi et al., 2020; Zhang et al., 2020d). As reported earlier, metal ions with smaller ionic radius and higher degree of electronegativity adsorbs faster than metal ions with larger ionic radius and lower electronegativity (Huang et al., 2020). The ionic radius of Pb(II), As(V) and Cd(II) are 0.98, 0.46 and 0.78 Å (Huang et al., 2020; Pawar et al., 2018), indicating that perhaps As(V) and Cd(II) with the possibly smaller ionic radii may diffuse ahead of Pb(II) into the inner surface of MWCNTs-KOH@NiNPs. In terms of electronegativity, Pb(II) has the highest value of 2.33, compared to 2.18 and 1.69 for As(V) and Cd(II) (Kharrazi et al., 2020; Pawar et al., 2018). Although the removal efficiency of As(V) ion was superior to Cd(II) at the various initial concentrations and temperatures due to its smaller ionic radius and higher electronegativity, Pb(II) ion with higher electronegativity recorded better penetration to the pores of the adsorbent and improved removal efficiency than both As(V) and Cd (II), respectively. Additionally, higher electronegative metals exert strong attraction to the lone pair electrons in the hydroxyl (—OH) and carboxyl (—COOH) functional groups (Huang et al., 2017). Except for Pb(II), the observed As(V) and Cd(II) removal effectiveness was favored by smaller ionic radius and higher electronegativity. Overall, the heavy metals removal efficiency by the exposed reactive surface sites of MWCNTs-KOH@NiNPs at the different initial concentrations were preferential to Pb(II) followed by As(V) and Cd(II).

The kinetics of the adsorption process was evaluated to determine the time-dependent performance of Pb(II), As(V) and Cd(II) uptake using MWCNTs-KOH@NiNPs. Therefore, the kinetic data from the experiments were fitted to the linear and nonlinear PFO, PSO and Elovich model to evaluate their suitability and significance towards the metal ions removal. The fitted curves and plots of the kinetic data using the nonlinear and linear equations are depicted in Figs. 4(b–d) and S1–S4. Similarly, the kinetic parameters, correlation coefficients and error

Table 1
Comparison of MWCNTs-KOH@NiNPs with the various adsorbents in the literature towards Pb(II), As(V) and Cd(II) adsorption.

Adsorbent	Surface area (m^2 g^{-1})	Adsorption capacity (mg/g)			Isotherm model	Kinetic model	Initial conc. (mg/L)	pH	Contact time (min)	Adsorbent dosage (mg/L)	Temp. (K)	Ref.
		Pb (II)	As(V)	Cd (II)								
Ash/GO/Fe_3O_4	858	47.2	–	43.7	Langmuir	PSO[a]	10	6	60	1000	298	(Pelalak et al., 2021)
MgC600	32.2	–	–	72.1	Langmuir	PFO[b]	500	5	1440	800	303	(Zhang et al., 2021b)
BCTD	62.8	–	118.1	72.6	Langmuir	PSO	100	5	240	100	298	(Luo et al., 2019)
$CaTiO_3$	–	261.8	–	82.6	Langmuir	PSO	280/750	6	120	1000	293	(Hang et al., 2019)
CABs-MO	–	–	63.6	31.2	Langmuir	PSO	100	6.5	720	1000	298	(Shim et al., 2019)
Fe_3O_3@PDA	14.2	–	–	21.6	Freundlich	PSO	20	7	120	20	298	(Lei et al., 2019)
Fe_3O_3	–	9.0	25.9	25.8	Langmuir	PSO	20	5.5	120	5000	298	(Lung et al., 2018)
BC-MnO_3	181.9	351.4		151.4	Langmuir	PSO	150	4.5	1440	25	298	(Zhang et al., 2020a)
CuONps	–	97.0	–	–	Freundlich	PSO	5	4.5	120	1000	298	(Zaidi et al., 2021)
PSF/HINM	195.8	–	41.1	–	Freundlich	PSO	100	7	720	1000	298	(Nasir et al., 2019)
PANI-NSA@Ni°CNs	49.8	434.7	–	–	Langmuir	PSO	150	5	90	500	288	(Bhaumik et al., 2020)
CNT-TRI		15.9			Freundlich	IPD[c]	5	6	180	30	298	(Albakri et al., 2018)
CSC@SDBC	53.2	228.7	–	–	Redlich-Peterson	PSO	50	5.5	60	–	303	(Ifthikar et al., 2020)
$ZrO(OH)_2$/CNTs	126	–	124.6		Langmuir	PSO	50	7	720	50	298	(Liu et al., 2018a)
MWCNTs-OCH_2CO_2H	1172	–	250.0	–	Langmuir	PSO	92	6	60	30	323	(Egbosiuba et al., 2020)
Fe-MWCNT			250.0		Freundlich	PFO	10	7	1320	200	318	(Alijani and Shariatinia, 2017)
$MnFe_2O_4$NPs	81.1		27.7		Freundlich	PSO	40	8	240	400	293	(Martínez, Vargas et al., 2018)
MWCNTs-KOH@NiNPs	1242	481.0	440.9	415.8	Langmuir	PSO	100	5.5	30	40	303	This study

[a] Pseudo-second order.
[b] Pseudo-first order.
[c] Intraparticle diffusion.

values determined from the nonlinear and linear plots are summarized in Table S1. The observed higher coefficient of determination (R^2) values and subsequently lower error (SSE and X^2) values of the PSO kinetic model compared to the PFO and Elovich kinetic model revealed that the former showed better fitness to predict the experimental data. Additionally, the actual adsorption capacity showed good correspondence with the calculated adsorption capacity from both nonlinear and linear PSO models. Therefore, the kinetic study for the uptake of investigated ions (Pb(II), As(V) and Cd(II)) applying MWCNTs-KOH@NiNPs composite were best suited with PSO model, referring to the mechanism of the adsorption process being driven primarily by chemisorption.

3.3.3. Adsorbent dosage effect

The adsorbent dosage effect on the removal of Pb(II), As(V) and Cd (II) on MWCNTs-KOH@NiNPs composite was conducted as shown in Fig. 5a. An obvious rapid increase in Pb(II), As(V) and Cd(II) ions adsorption onto MWCNTs-KOH@NiNPs was observed with increase in the amount of adsorbent from 5 to 40 mg/L.

Meanwhile, Fig. 5a revealed the increasing trend of the uptake of As (V) (from 151.5 to 212.7 mg/g), Cd(II) (from 116.3 to 190.6 mg/g) and Pb(II) (from 201.0 to 255.8 mg/g) at temperature of 303 K, which may be associated to increase in the amount of sites available for adsorption. In contrast, further increment in dosage of adsorbent up to 50 mg/L at the respective temperatures of 303, 313 and 323 K displayed a noticeable decline on the adsorption capacity of ions owing to the aggregation of adsorption sites on the MWCNTs-KOH@NiNPs surface (Jun et al., 2019). Consequently to the maximum adsorption capacity reported in this study, the optimum adsorbent dosage of 40 mg/L was established for further investigation. Pb(II) ions showed higher adsorption than As(V) and Cd(II) at the various temperatures and may be linked to its higher degree of electronegativity. Importantly, the adsorption capacity of Pb(II), As(V) and Cd(II) ions suggests overt dependence of the adsorption phenomena on the surface functional moieties of MWCNTs-KOH@NiNPs due to the presence of strong electrostatic attraction. Except for the work of Lei et al. (2019), Zhang et al. (2020a), Albakri et al. (2018) and Egbosiuba et al. (2020) that reported an adsorbent dosage of 20, 25, 30 and 30 mg/L, the optimum dosage (40 mg/L) obtained in this study was remarkably smaller than others presented in Table 1. The smaller amount of the nanocomposite required for optimum removal of the metal ions compared to other studies may be due to the surface properties, functional groups, thermal stability, morphological and structural network of the nanocomposites.

3.3.4. Initial metal concentration and isotherm study

The influence of ion initial concentrations (Pb(II), As(V) and Cd(II)) on the adsorption capacity of MWCNTs-KOH@NiNPs was studied as presented in Fig. 5(b–d). Accordingly, the sorption capacity of sorbent material (MWCNTs-KOH@NiNPs) towards Pb(II), As(V) and Cd(II) at the temperature (303 K) increased from 148.7 to 440.1 mg/g,

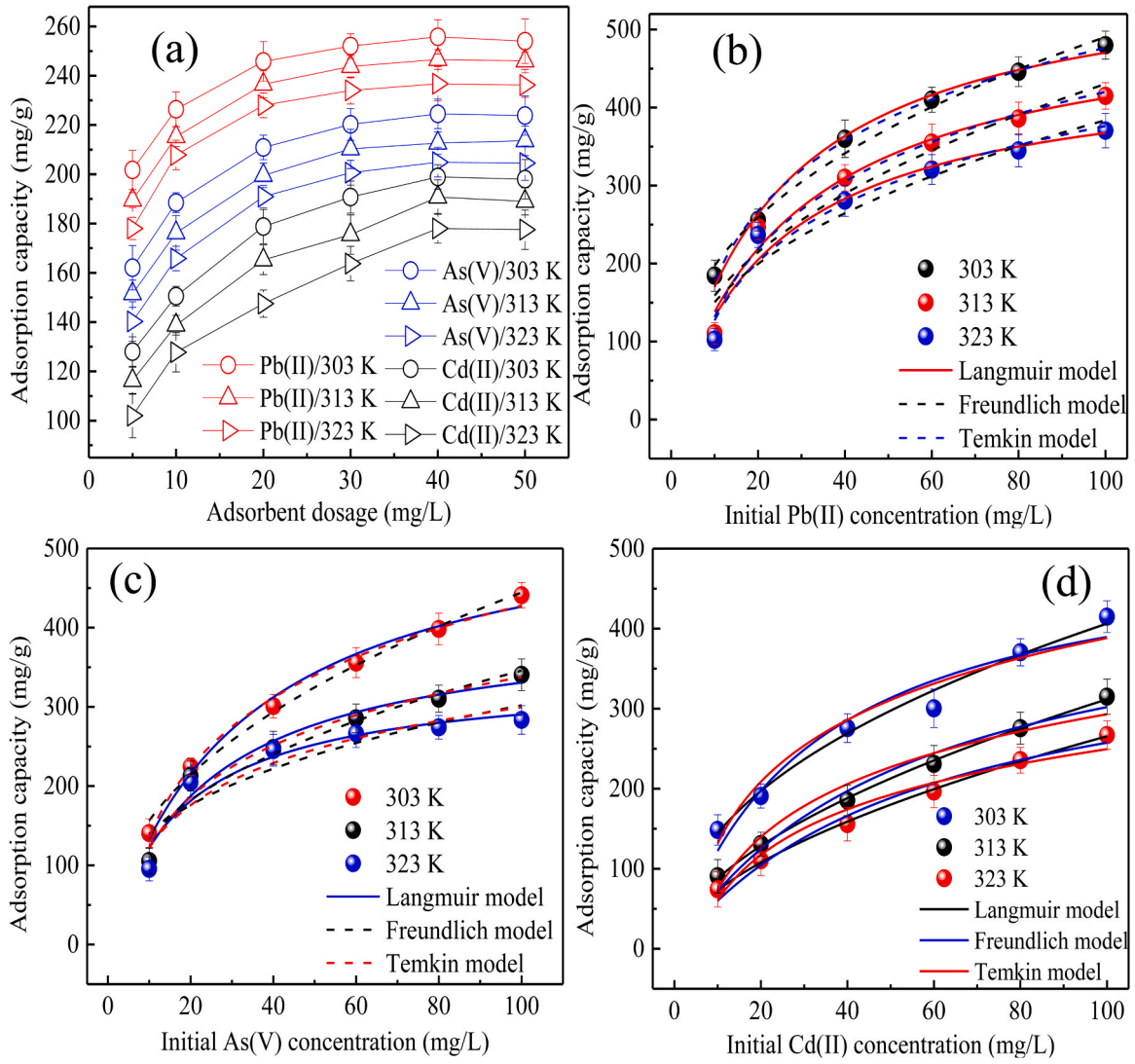

Fig. 5. (a) The adsorbent dosage effect on the Pb(II), As(V) and Cd(II) adsorption at different temperatures by MWCNTs-KOH@NiNPs at pH equal to 5.5, initial metal concentration of 20 mg/L and contact time of 60 min; the equilibrium isotherm plots of (b) Pb(II); (c) As(V) and (d) Cd(II) adsorption by MWCNTs-KOH@NiNPs and nonlinear fitting of isotherm data with Langmuir, Freundlich and Temkin models (pH equal to 5.5 and contact time of 60 min (20 mg/L), 40 min (60 mg/L) and 30 min (100 mg/L)).

140.5–415.3 mg/g and 184.4–480.0 mg/g, respectively. Generally, the process adsorption capacity of metal ions increases as the initial concentration increases, thereby exerting positive influence on the driving force of the adsorption process (Zhao et al., 2020). Particularly, the surface of MWCNTs-KOH@NiNPs accommodates large amount of available adsorption sites that were already protonated. Going forward, the active sites become steadily occupied and thus, lowering the adsorption capacity to attain equilibrium. It can also be noted from Fig. 5(b–d) that the adsorption capacity of ions applying MWCNTs-KOH@NiNPs decreased with increase in temperature, indicating the adsorption process was exothermic. Therefore, the adsorption capacities of MWCNTs-KOH@NiNPs for Pb(II), As(V) and Cd(II) adsorption were studied at different temperatures, namely 303, 313 and 323 K resulted in Pb(II) (480.0, 415.2 and 370.4 mg/g), As(V) (440.1, 340.5 and 283.6 mg/g) and Cd(II) (415.3, 315.0 and 267.0 mg/g) adsorption capacities.

Further explanation on the adsorption properties of MWCNTs-KOH@NiNPs towards Pb(II), As(V) and Cd(II) were conducted using (i) Langmuir, (ii) Freundlich and (iii) Temkin isotherm models using experimental data. Generally, Langmuir isotherm primarily assumes the concept of the adsorption process that happens on a homogeneous surface and is oriented as a monolayer, while Freundlich isotherm model happens on a heterogeneous surface in a form of a multilayer adsorption process (Zhao et al., 2020). On the other hand, Temkin isotherm model evaluates the interaction of adsorbent and the investigated metal ions (Zhang et al., 2020d). The nonlinear and linear Langmuir, Freundlich and Temkin isotherm model fitted plots in relation to the isotherm data are presented in Figs. 5(b–d) and S4–S12, respectively. In addition, isotherm parameters from the nonlinear and linear regression analysis of the empirical data at the temperatures 303, 313 and 323 K are presented in Table S2.

Notably, Langmuir isotherm model best described the isotherm data due to the higher R^2 and lower SSE and X^2 values for both the nonlinear and linear Langmuir model, compared to Freundlich and Temkin models. Above all, the result suggests the governance of Pb(II), As(V) and Cd(II) uptake by a monolayer adsorption process onto the uniform surface of MWCNTs-KOH@NiNPs. The maximum adsorption capacity for the nonlinear Langmuir fitting at 303, 313 and 323 K are 482.6, 418.7 and 371.3 mg/g for Pb(II), 441.1, 340.6 and 284.7 mg/g for As(V) and 416.2, 317.1 and 268.1 mg/g for Cd(II). For the linear Langmuir model, the maximum adsorption capacities were obtained for Pb(II) (481.0, 416.1 and 370.6 mg/g), As(V) (440.9, 342.8 and 285.1 mg/g)

and Cd(II) (415.8, 318.3 and 270.5 mg/g) at the various temperatures of 303, 313 and 323 K, respectively. Clearly metal ion adsorption capacity decreased with simultaneous increase in process temperature, thereby implying an improvement in the chemical interaction of the active binding sites of the MWCNTs-KOH@NiNPs with Pb(II)/As(V)/Cd(II) at reduced temperature. Then again, the adsorption rate (K_L) decreased with increase in temperature, signifying the superior affinity of MWCNTs-KOH@NiNPs towards Pb(II), As(V) and Cd(II) adsorption at lower temperatures. In Langmuir isotherm, the R_L value between $0 < R_L < 1$ depict a favorable adsorption (Zhao et al., 2020) and as such the values obtained in this study fall between 0 and 1, thereby validating that the adsorption process is occurring favorably. Furthermore, Freundlich isotherm constant, n_F value in the range $1 < n_F < 10$ depict a beneficial adsorption process (Lung et al., 2018). Since the n_F values in this study ranged between 2.127 and 6.780, the adsorption of ions (Pb (II), As(V) and Cd(II)) applying MWCNTs-KOH@NiNPs demonstrated a favorable chemical adsorption. Overall, Temkin isotherm constant (B) shown in Table S2 was observed to decrease with increase in temperature, thereby confirming the exothermicity of metal ions adsorption applying MWCNTs-KOH@NiNPs. The chemical nature of the adsorption process of Pb(II), As(V) and Cd(II) by the adsorbent corroborated with the prediction of pseudo-second order kinetic model. Additionally, the adsorption capacities of the various adsorbents for Pb(II), As(V) and Cd (II) adsorption in relation to this study used sorbent are compared as listed in Table S2. It can be evidently concluded that the maximum process adsorption capacities of the developed adsorbents were found smaller than that reported in this study.

3.3.5. *Temperature and thermodynamic study*

The influence of the applied temperature on the adsorption process of Pb(II), As(V) and Cd(II) onto MWCNTs-KOH@NiNPs was studied and presented in Fig. 6a. The results indicate that the adsorption capacity of sorbent material (MWCNTs-KOH@NiNPs) of Pb(II), As(V) and Cd(II) decreased with increase in temperature from 303 to 343 K. According to Fig. 6a, the adsorption capacity of the metal ions decreased from 480.0 to 210.6 mg/g for Pb(II), 440.1 to 175.2 mg/g for As(V) and from 415.3 to 141.8 mg/g for Cd(II), respectively as the temperature increased (from 303 to 343 K). The evident reduction in the efficiency of adsorption signify the unfavorable removal of Pb(II), As(V) and Cd(II) applying MWCNTs-KOH@NiNPs at elevated temperature. This may be due to the functional groups alteration which occurs at high temperatures, thereby modifying the sorbent surface chemistry and as such decreasing quantity of available active sites for metal ions adsorption (Mohammadreza et al., 2021). In addition, increase in temperature decreases the boundary

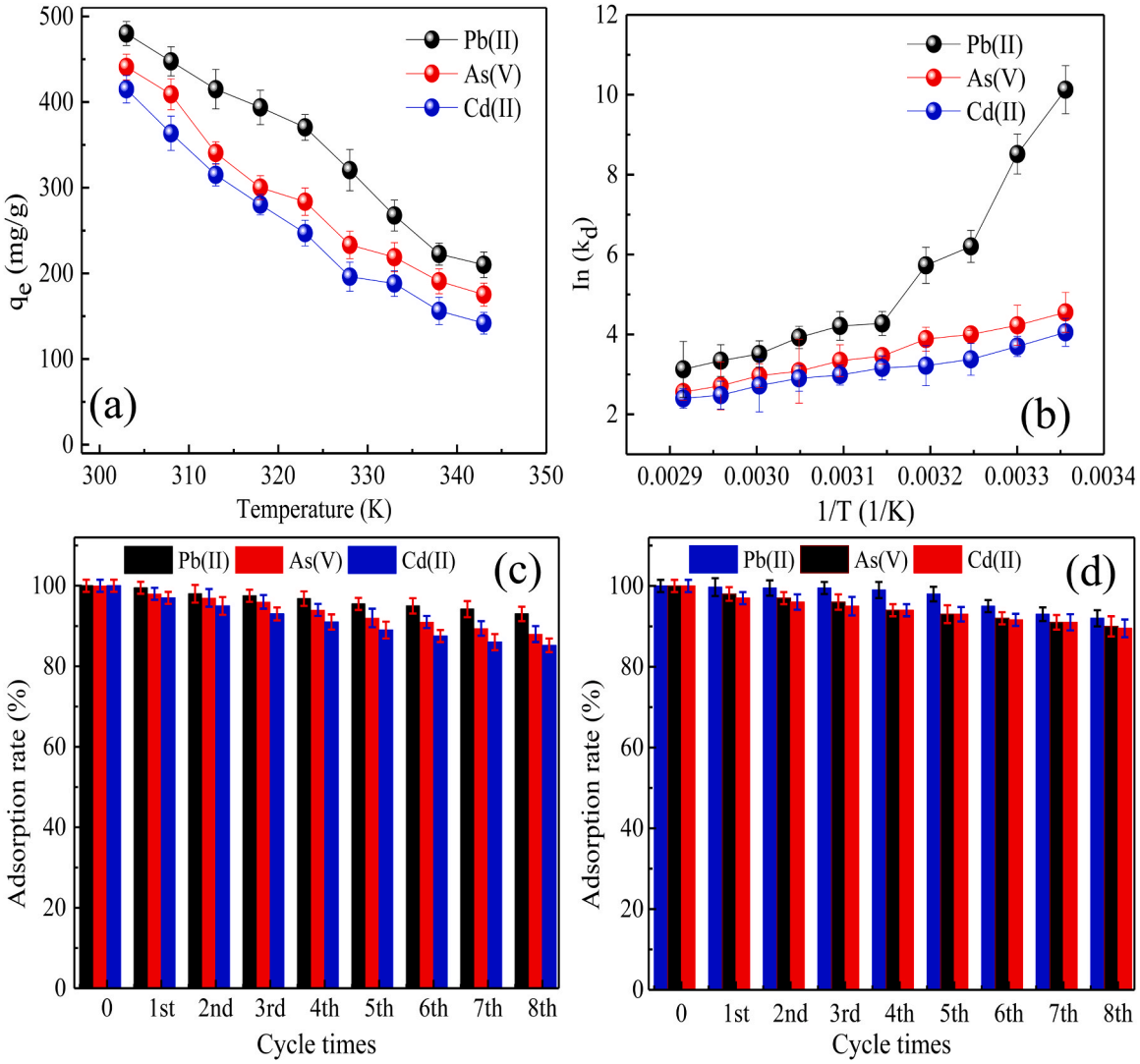

Fig. 6. (a) Temperature effect on metal ion adsorption applying MWCNTs-KOH@NiNPs at pH equal to 5.5, adsorbent dosage of 40 mg/L and contact time of 30 min and (b) the plot of $\ln(k_d)$ against $1/T$; adsorption rate of MWCNTs-KOH@NiNPs towards Pb(II), As(V) and Cd(II) as a function of adsorption-desorption cycles in (c) a batch and (d) fixed bed systems (pH equal to 5.5, adsorbent dosage of 40 mg/L, contact time of 30 min and temperature of 303 K).

layer thickness because of high tendency of Pb(II)/As(V)/Cd(II) ions to escape from the sorbent surface to the bulk of the solution, thus reducing the adsorption efficiency (Mohammadreza et al., 2021).

To further investigate the observed sorption process, the thermodynamic related parameters for Pb(II), As(V) and Cd(II) adsorption on MWCNTs-KOH@NiNPs were estimated by the fitted data shown in Fig. 6b. The evaluated thermodynamic related parameters such as, (i) Gibbs free energy (ΔG°), (ii) enthalpy change (ΔH°) and (iii) entropy change (ΔS°) are presented in Table S3. It can be seen that all values of thermodynamic related parameters were all negative. Thus, the ΔG° points to the viability of the adsorption process and the spontaneity of Pb(II)/As(V)/Cd(II) ions sorption on the surface of MWCNTs-KOH@NiNPs. In addition, the ΔH° validates the exothermic nature of the current adsorption process, revealing that the adsorption capacity will decrease as temperature increases. Then again, the ΔS° demonstrates reduction in randomness at the solid-liquid interface (Bhaumik et al., 2020). In all, the thermodynamic results showed strong corroboration with the results of adsorption kinetics.

3.4. Continuous flow adsorption experiments

Further corroboration of the industrial application of MWCNTs-KOH@NiNPs towards investigated ions (Pb(II), As(II) and Cd(II)) adsorption prompted the incorporation of fixed-bed column adsorption. Accurate parameters effects and effective prediction of breakthrough curves in dynamic column systems enhance better design of facilities, future operations and costs of maintenance (Ifthikar et al., 2020). Therefore, fixed-bed studies were performed at various bed heights (2, 3 and 4 cm), inlet metal ion concentrations (20, 60 and 100 mg/L) with flow rates (5, 6 and 7 mL/min). Consequently, the plots of the breakthrough curves and the determined operational parameters are presented in Figs. S13–S15 and Table 2, respectively.

3.4.1. Bed height influence on the breakthrough curve

For fixed-bed based columns, bed height is one of the most principal parameter. Therefore, bed height effect on the breakthrough curve was studied at a constant solution pH equal to 5.5 and temperature of 303 K as shown in Fig. S13. It can be seen from the result that increase in bed height extended the breakthrough and saturation time due to the growth in surface area and available binding sites for Pb(II), As(II) and Cd(II) adsorption associated with the large amount of sorbent in the column, thereby decreasing the breakthrough curve slope and widening the mass transfer zone (Franco et al., 2020). According to Table 2, once the bed height was increased (from 2 to 4 cm), the breakthrough time (t_b), saturation time (t_e), volume of the effluent (V_{eff}), the total adsorbed amount of metal ions (q_{total}), length of mass transfer zone (L_{MTZ}), the removal efficiency (R%) and empty bed contact time (EBCT) also increased. The trend of this result is an indication that a higher bed height provides more adsorption sites and contact time for ion adsorption (Mohammadreza et al., 2021). In contrast, the equilibrium adsorption capacity (q_e) decreased with increase in the bed height owing to the lower ratio of Pb(II)/As(V)/Cd(II) ions and the available adsorption sites (Aichour et al., 2019; Franco et al., 2020). A similar observation was elaborated by Ifthikar et al. (2020) and Yahya et al. (2020) during fixed-bed adsorption studies on metal ions.

3.4.2. Inlet concentration influence on the breakthrough curve

In this study, the impact of the inlet concentrations (20, 60 and 100 mg/L) of Pb(II), As(II) and Cd(II) on the breakthrough curves was studied at conditions of a constant bed height and flow rate of 4 cm and 5 mL/min, respectively as shown in Fig. S14 and Table 2. Remarkably at lower inlet Pb(II)/As(II)/Cd(II) concentrations, the values for the t_b and t_e were higher, thereby allowing for the treatment of large volume of effluent (V_{eff}) and the corresponding higher R%, EBCT and C_e of ions. The trend of this result could be associated to lower driving force for the possible mass transfer at lower inlet concentration, thereby requiring a longer time to transport the ions within the column, from the liquid to the solid and along the solid (Franco et al., 2020). Hence, slower diffusion of Pb(II)/As(II)/Cd(II) ions into the MWCNTs-KOH@NiNPs was demonstrated at low inlet concentration (20 mg/L). In contrast, an obvious shift in breakthrough curves towards the origin was observed at higher Pb(II)/As(II)/Cd(II) inlet concentration. Fig. S14 revealed that the slope of the breakthrough curve becomes steeper with the simultaneous increase of the inlet metal concentration, thus reducing the breakthrough and saturation time (Ang et al., 2020). Above all, the total adsorbed Pb(II)/As(II)/Cd(II) (q_{total}), L_{MTZ}, q_e and C_e increased as the inlet metal concentration increases. This phenomenon may be linked to the presence of larger driving force for mass transfer and abundant active sites at higher inlet metal concentration (100 mg/L), which causes rapid saturation of the adsorbent bed (Gupta and Garg, 2019). Previously, researchers have reported a similar effect of inlet metal concentration on fixed-bed based adsorption process of metal ions on different adsorbents (Bo et al., 2020; Ghasemi et al., 2019; Hayati et al., 2018; Zhang et al., 2020b).

Table 2
Continuous column and breakthrough curve parameters for MWCNTs-KOH@NiNPs composite adsorption towards Pb(II), As(V) and Cd(II).

Adsorbates	C_o (mg/L)	Q (mL/min)	Z (cm)	t_b (min)	t_e (min)	V_{eff} (L)	q_{total} (mg)	L_{MTZ} (cm)	q_{eq} (mg/g)	m_{total} (mg)	R (%)	EBCT (min)	C_e (mg L^{-1})
Pb(II)	20	5	2	720	2600	13.0	323.8	1.5	323.8	325	99.64	2.6	0.090
	20	5	3	1400	3000	15.0	373.9	1.6	249.3	375	99.72	3.0	0.070
	20	5	4	1800	3400	17.0	424.2	1.9	212.1	425	99.80	3.4	0.050
	60	5	4	960	2600	13.0	648.0	2.5	324.0	650	99.70	3.0	0.150
	100	5	4	480	2000	10.0	1298.0	3.0	649.0	1000	99.80	2.0	0.200
	20	6	4	1200	3000	18.0	447.7	2.4	223.8	450	99.68	3.0	0.130
	20	7	4	720	2200	15.4	383.5	2.7	191.7	385	99.60	2.2	0.100
As(V)	20	5	2	720	2400	12.0	299.9	1.4	299.9	300	99.97	2.4	0.006
	20	5	3	1400	2800	14.0	349.9	1.5	233.3	350	99.98	2.8	0.005
	20	5	4	1800	3200	16.0	399.9	1.8	200.0	400	99.99	3.2	0.002
	60	5	4	1200	2800	14.0	699.8	2.3	349.9	700	99.98	2.8	0.009
	100	5	4	720	2400	12.0	1199.8	2.8	590.9	1200	99.99	2.4	0.010
	20	6	4	1200	2800	16.8	429.8	2.3	209.9	420	99.97	2.8	0.007
	20	7	4	480	2000	14.0	349.9	3.0	174.9	350	99.96	2.0	0.008
Cd(II)	20	5	2	720	2400	11.00	299.4	1.4	299.4	300	99.80	2.4	0.050
	20	5	3	1200	3000	13.00	374.6	1.8	249.7	375	99.88	3.0	0.030
	20	5	4	1600	3400	15.00	424.8	2.1	212.4	425	99.96	3.4	0.010
	60	5	4	960	3000	15.00	749.1	2.7	374.6	750	99.88	3.0	0.060
	100	5	4	480	2600	13.00	998.7	3.3	452.4	1300	99.90	2.6	0.100
	20	6	4	960	3000	15.00	418.7	2.7	224.4	450	99.72	3.0	0.070
	20	7	4	480	2400	13.80	326.7	3.2	209.3	420	99.68	2.4	0.080

3.4.3. Flow rate influence on the breakthrough curve

To study the flow rate influence on the breakthrough curve, bed height of MWCNTs-KOH@NiNPs, inlet Pb(II)/As(II)/Cd(II) ions concentrations, initial solution pH and temperature were kept constant at 4 cm, 20 mg/L, 5.5 and 303 K, while the flow rate was changed from 5, 6 to 7 mL/min. The results of the breakthrough curves and determined fixed-bed parameters are presented in Fig. S15 and Table 2. The breakthrough curves shown in Fig. S15 revealed that the increase in flow rate shortened the breakthrough time, thereby producing steeper curves. Hence, breakthrough occurs rapidly with 7 mL/min compared to the lower flow rates (Aichour et al., 2019). According to Table 2, increasing the flow rate led to the observed decrease in the values of t_b, t_e V_{eff}, q_{total}, EBCT and C_e for Pb(II), As(II) and Cd(II) ions. The possible reason for this behavior may be owing to limited contact (lower residence time) when a higher flow rate was used and the corresponding diffusion related limitations of metal ions into the pores of the adsorbent material (Franco et al., 2020). The decline in EBCT due to increase in flow rate validate that a higher interaction time exist between the MWCNTs-KOH@NiNPs and Pb(II)/As(II)/Cd(II) solution at low flow rate than at high flow rate (Fallah and Taghizadeh, 2020). Therefore, decrease in removal efficiency indicated the favorability of low flow rate, while decrease in flow rate enhanced the adsorption capacity (Mohammadreza et al., 2021). These are consistent with other literature reports (Ghasemi et al., 2019; Hayati et al., 2018; Mohammadreza et al., 2021; Yahya et al., 2020).

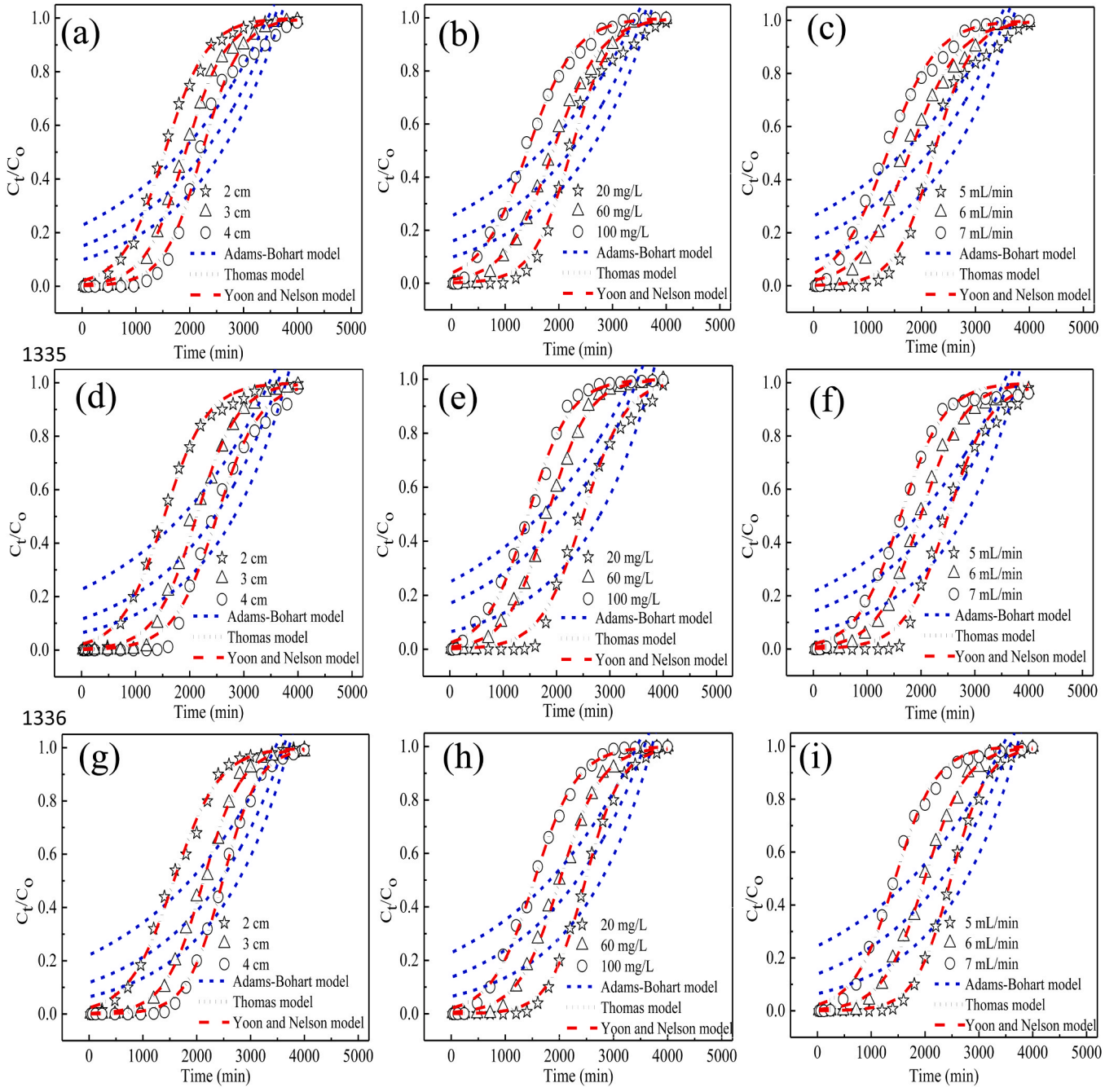

Fig. 7. Experimental and modeling curves for (a–c) Pb(II); (d–f) As(V) and (g–i) Cd(II) adsorption by MWCNTs-KOH@NiNPs using various models at different bed heights, inlet concentrations and flow rates.

3.5. Kinetic modeling of fixed-bed adsorption data

To further describe the breakthrough curves from column experiments using MWCNTs-KOH@NiNPs, the system was modeled using nonlinear and linear Adams-Bohart, Thomas and Yoon-Nelson equations. Predicted breakthrough curves and determined kinetic parameters using the linear model equation are presented in Figs. S16–S21 and Table S4, while those of the nonlinear equations are demonstrated in Fig. 7 and Table S5, respectively.

Adams–Bohart model is based on the fact that the adsorption process occurs at equilibrium condition is not rapid and applied in the description of the initial section of the breakthrough curves (Mohammadreza et al., 2021). Breakthrough curves for the linear and nonlinear expressions and their determined parameters are presented in Figs. S16, S17, 7, Tables S4 and S5, respectively. In view of the obtained model parameters, Adams–Bohart kinetic constant (K_{AB}) increased with the simultaneous increase in bed height, while an increase in the inlet metal concentrations and flow rates reduced the value of K_{AB} in both the linear and nonlinear regression analysis. It is evident from the result that the saturation concentration (N_0) decreased with the same time increase in bed height, while the increase in inlet metal concentration and flow rate increased the value of N_0. The observed unfavorable effect of the bed height on the N_0 indicate a decline in the adsorption process (de Franco et al., 2018). Also, the volume of Pb(II)/As(V)/Cd(II) solution entering the adsorption column was higher, thence resulting to faster bed saturation due to higher metal concentration and lengthened flow rate (Aichour et al., 2019). Moreover, the regression coefficient (R^2) (0.53–0.87) revealed the non-suitability of Adams–Bohart model to predict the breakthrough curve for Pb(II)/As(V)/Cd(II) adsorption onto MWCNTs-KOH@NiNPs. Similar findings have also been reported by Fallah and Taghizadeh (2020) for the removal of metal ions.

Thomas model is based on specific conditions of plug flow based behaviors in the sorbent bed, Langmuir isotherm, pseudo-second order kinetics and a constant separation factor that can be applied to a favorable and unfavorable isotherm (Gupta and Garg, 2019). Typically, both linear and nonlinear expressions of Thomas model were applied to predict the systems ultimate adsorption capacity (q_o) of MWCNTs-KOH@NiNPs and the process rate constant (K_{TH}) for the removal of Pb(II)/As(II)/Cd(II) in the adsorption column. The nonlinear and linear breakthrough curves of Thomas model are shown in Figs. 7, S18 and S19, while the related to the model parameters are presented in Tables S4 and S5. According to the result, it was discovered that the increase in bed height and inlet metal concentration decreased the value of Thomas rate constant (K_{TH}) and increased the value of saturation adsorption capacity (q_o). This may be because of the stronger driving force of the adsorption process due to the concentration differences of the inlet and adsorbed metal ions on the adsorbent surface, thereby increasing the adsorption capacities at higher bed height and inlet concentration (Fallah and Taghizadeh, 2020). On the other hand, increase in flow rate provokes decreased both the values of the K_{TH} and q_o, respectively. Based on the R^2, the best model fitting for removal efficiency of the metal ions were in the sequence Pb(II) > As(V) > Cd(II) in both the linear and nonlinear relationships. Equally, the experimental and theoretical adsorption capacities of Pb(II), As(V) and Cd(II) showed significant similarity in both linear and nonlinear model equations, thus validating the suitability of Thomas model.

Generally, Yoon–Nelson model was employed to model the empirical data and the obtained results are presented in Figs. 7, S20 and S21. Also, the determined constants and R^2 values are mentioned in Tables S4 and S5 for the linear and nonlinear representations, respectively. As shown in Tables S4 and S5, Yoon–Nelson constant (K_{YN}) decreased as the bed height increased and also increased as the inlet metal concentration and flow rate was increased. The trend of this result may be ascribed to the increased concentration differences through the fixed-bed that correspond to increase in K_{YN} values (Ang et al., 2020). In this case, MWCNTs-KOH@NiNPs bed height (2 cm) reached saturation at shorter time because of higher inlet Pb(II), As(V) and Cd(II) concentration and flow rate. However, the required time to attain 50% breakthrough ($t_{0.5}$) increased with the increase in applied bed height, but declined as the inlet metal concentration and flow rate was increased. Apparently, both Thomas and Yoon–Nelson models can be effectively explored to predict the breakthrough curve of Pb(II), As(V) and Cd(II) adsorption. Remarkably, both Thomas and Yoon–Nelson models exhibited strong inter-correlation coefficient (R^2) and obtained similar values for breakthrough curve prediction in the absorption process. The successful prediction of experimental data by Thomas and Yoon–Nelson models had been explored previously (Aichour et al., 2019; Ang et al., 2020; de Franco et al., 2018; Gupta and Garg, 2019; Ifthikar et al., 2020).

Furthermore, analysis of variance (ANOVA) was used for the contributions of (i) bed height, (ii) inlet concentration and (iii) flow rate on the adsorption capacity of MWCNTs-KOH@NiNPs towards ions. Accordingly, the results for the sum of square (SS) as well as mean square (MS) and ultimately F-value are shown in Table S6. Specifically, higher bed heights, lower inlet concentration and flow rate had higher F-values, thereby indicating their percentage contributions in fixed-bed adsorption. Overall, Thomas and Yoon–Nelson models produced higher F-values for Pb(II), As(V) and Cd(II) adsorption, thus confirming a proper prediction of the breakthrough curve, compared to Adams–Bohart model. The findings of this study show that the data predicted by Thomas and Yoon–Nelson model best fitted the experimental breakthrough curves. Therefore, higher bed height, lower inlet metal concentration and smaller flow rate improved significantly the efficient adsorption of MWCNTs-KOH@NiNPs towards studied ions in a continuous column based adsorption process.

3.6. Adsorption mechanism

Further study was carried out on the mechanism of Pb(II), As(V) and Cd(II) adsorption from wastewater samples applying MWCNTs-KOH@NiNPs using XRD and FTIR analysis. Accordingly, the XRD pattern of MWCNTs-KOH@NiNPs after reaction with Pb(II), As(V) and Cd(II) displayed in Fig. 8a elucidates clear differences in diffraction peaks in contrast with the diffraction peaks (Fig. 2a) before the reaction. Although the characteristic peaks of Ni nanoparticles and MWCNTs at 2θ values 37.50° (111), 43.50° (200), 62.89° (220), 75.40° (311), 79.40° (222) and 26.27° (002), 50.87° (102) and 77.60° (311) were still observed. Remarkably, additional diffraction peaks appeared at 2θ of 14.96°, 30.17°, 33.18°, 36.20° and 53.99° which may be attributable to the crystalline peaks associated with the adsorbed metallic Pb, As and Cd (Bhaumik et al., 2020; Qu et al., 2020). From the XRD result, it can be suggested that the oxidation of Ni nanoparticles into Ni(II) at higher pH (~ 5.0) may be responsible in the efficient removal of Pb(II), As(V) and Cd(II).

The functional groups that participated in the adsorption of ions were estimated through the FTIR spectra of MWCNTs-KOH@NiNPs after adsorption as shown in Fig. 8b. From the FTIR spectra result, it is evident that additional spectra appeared at 624, 1000 and 1126 cm^{-1} after adsorption which indicated the involvement of carbonyl, carboxyl and hydroxyl functional groups towards the removal of ions (Ifthikar et al., 2020). In addition, the strength of the bands at 692, 876 and 3446 cm^{-1} appeared weakened after ion adsorption, showing the interaction of the functional groups/moieties and the metal ions (Qu et al., 2020). The mechanism of the adsorption of MWCNTs-KOH@NiNPs towards Pb(II), As(V) and Cd(II) appears to involve electrostatic attraction, pore diffusion, complexation and ion exchange. The observed mechanism could be attributed to the metallic properties of NiNPs in reducing the hydrophobic nature of MWCNTs and enhancing the surface properties, functional groups, electronic configurations, morphological and porous structure of the nanocomposite towards enhanced removal of metal ions.

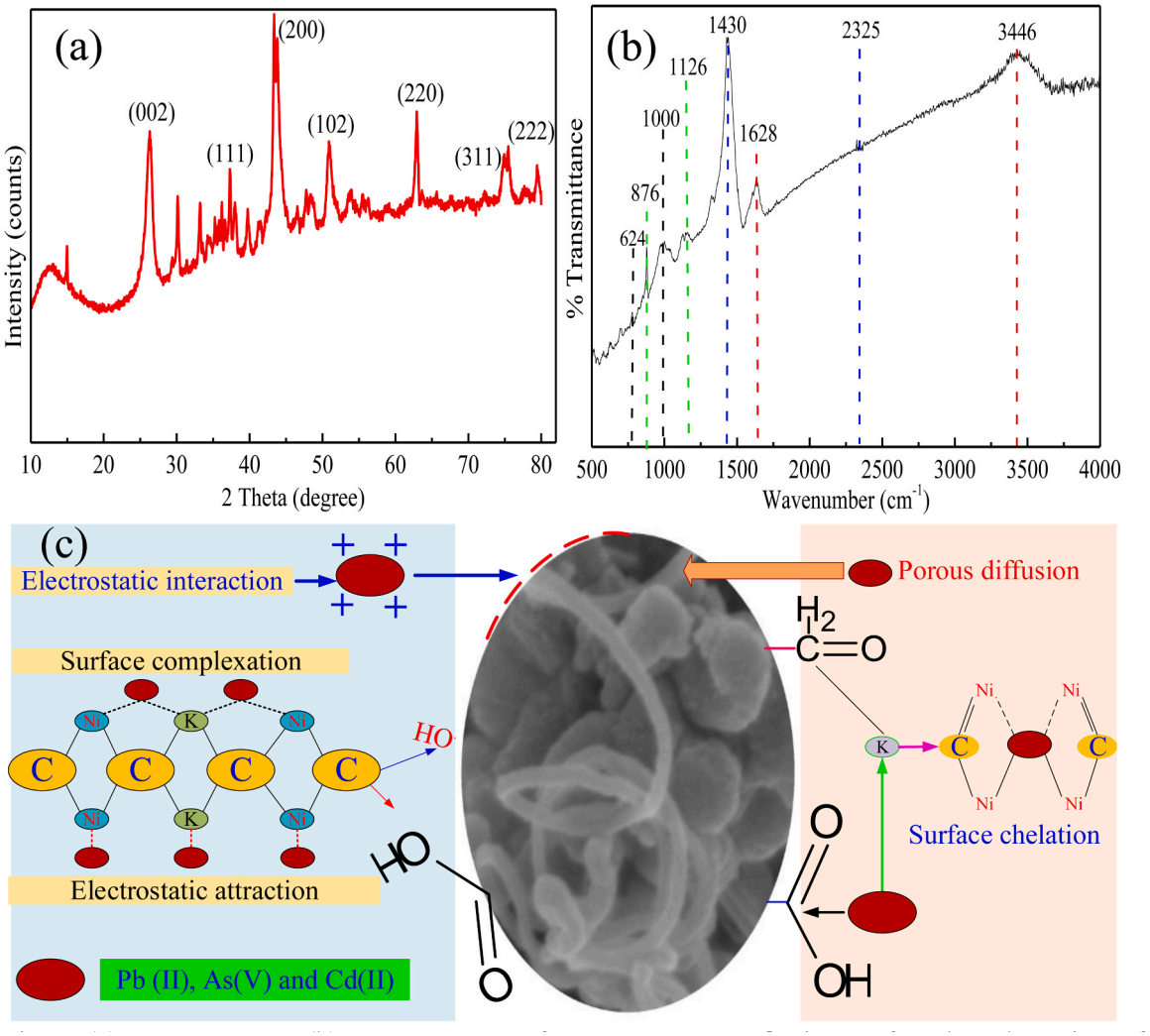

Fig. 8. (a) XRD pattern; (b) FTIR spectra of MWCNTs-KOH@NiNPs after the adsorption of Pb(II), As(V) and Cd(II) and (c) projected adsorption mechanisms of Pb(II), As(V) and Cd(II).

3.7. Regeneration and reusability

For practical application of adsorbents, regeneration and reusability had been adjudged the most important determining parameter towards the stability of the sorbents and reduction in the cost of the adsorbents. Thereupon, the desorption property of MWCNTs-KOH@NiNPs was evaluated for the batch and fixed-bed systems and the result presented in Fig. 6(c, d). It is evident from both Fig. 6c and d that after the recyclability of the adsorbent for 8 times, the adsorption rate reduced to approximately 80% in both batch and dynamic systems using the adsorbent. Similarly, the observed reduction in the adsorption rate of MWCNTs-KOH@NiNPs for Pb(II), As(II) and Cd(II) are 7%, 12% and 14.8% for batch and 8%, 10% and 10.5% for fixed-bed technique. The observed reduction in the adsorption rate after 8th adsorption cycle could be caused by the loss of materials and the adsorption sites occupied by the species of unreleased ions. In view of the high rate of adsorption and reuse ability of the adsorbent, the MWCNTs-KOH@NiNPs is a highly promising adsorbent for useful application in water treatment industry.

4. Conclusion

Herein, NiNPs were successfully prepared and incorporated onto the activated surface of MWCNTs to reduce the hydrophobicity and surface area increase, functional groups, morphology and porosity of the nanocomposite. The characterization of the produced NiNPs confirmed the successful assembly of the metallic nanoparticles with spherical structure in the nanocomposite. The EDS analysis revealed the presence of carbon, potassium, oxygen and NiNPs on the surface of the MWCNTs-KOH@NiNPs nanocomposite. The HRSEM, HRTEM, XRD, FTIR, TGA, surface analysis validated the morphological structure, tubular structural network, functional groups, crystalline nature, thermal stability and surface properties of NiNPs, MWCNTs-KOH and MWCNTs-KOH@NiNPs. Comparatively, MWCNTs-KOH@NiNPs showed higher surface area of 1242 $m^2\ g^{-1}$ in relation to MWCNTs-KOH (1230 $m^2\ g^{-1}$) and NiNPs (56 $m^2\ g^{-1}$). MWCNTs-KOH@NiNPs showed a higher adsorption capacity of 91.2 ± 8.7%, 88.5 ± 6.5% and 80.6 ± 5.8% towards Pb(II), As(II) and Cd(II) ions, compared to MWCNTs-KOH Pb(II) (68.4 ± 5.0%), As(V) (65.5 ± 4.2%) and Cd(II) (50.7 ± 3.4%) and NiNPs (Pb(II) (58.6 ± 4.1%), As(V) (46.8 ± 3.7%) and Cd(II) (40.5 ± 2.5%)). In the batch study, MWCNTs-KOH@NiNPs successfully removed the metal ions with maximum adsorption capacity of 481.0, 440.9 and 415.8 mg/g for Pb(II), As(V) and Cd(II) at the pH of 5.5, contact time of 30 min, adsorbent dosage of 40 mg/L, initial metal concentration of 100 mg/L and temperature of 303 K. More of Pb(II) ion were removed ahead of As(V) and Cd(II) at each adsorption condition. Langmuir isotherm predicted the equilibrium data better than Freundlich and Temkin models, while pseudo-second order kinetic model fitted

better than pseudo-first order and Elovich kinetic model. Thermodynamic data indicated the exothermic characteristics of the adsorption process. Furthermore, in the continuous column adsorption, the ions were efficiently removed at the conditions of higher bed height, higher inlet metal concentration and lower flow rate of 4 cm, 100 mg/L and 5 mL/min, respectively. Thomas model fitted the experimental data and followed closely by Yoon–Nelson model. Thus, the produced MWCNTs-KOH@NiNPs is a promising nanocomposite with multifunctional capacity to remove heavy metals from industrial wastewater at the optimal conditions described by the batch and fixed-bed systems.

CRediT authorship contribution statement

Titus Chinedu Egbosiuba: Conceptualization, Investigation, Methodology, Data curation, Writing – original draft, Writing – review and editing, Validation. **Michael Chika Egwunyenga:** Investigation, Methodology, Data curation. **Jimoh Oladejo Tijani:** Data curation, Writing – review and editing. **Saheed Mustapha:** Data curation, Methodology, Software. **Ambali Saka Abdulkareem:** Writing – review and editing, Resources, Supervision. **Abdulsalami Sanni Kovo:** Writing – review and editing, Resources, Supervision. **Vida Krikstolaityte:** Characterization, Writing – review & editing. **Andrei Veksha:** Writing – review and editing. **Michal Wagner:** Writing – review and editing, Software. **Grzegorz Lisak:** Writing – review and editing, Resources, Supervision.

Declaration of Competing Interest

The authors declare that they have no known competing financial interests or personal relationships that could have appeared to influence the work reported in this paper.

Appendix A. Supplementary information

Supplementary data associated with this article can be found in the online version at doi:10.1016/j.jhazmat.2021.126993.

References

Ahamed, A., Ge, L., Zhao, K., Veksha, A., Bobacka, J., Lisak, G., 2021. Environmental footprint of voltammetric sensors based on screen-printed electrodes: an assessment towards “green” sensor manufacturing. Chemosphere 278. https://doi.org/10.1016/j.chemosphere.2021.130462.

Ahmad, I., Siddiqui, W.A., Ahmad, T., Siddiqui, V.U., 2019. Synthesis and characterization of molecularly imprinted ferrite (SiO2@Fe2O3) nanomaterials for the removal of nickel (Ni2+ ions) from aqueous solution. J. Mater. Res. Technol. 8, 1400–1411. https://doi.org/10.1016/j.jmrt.2018.09.011.

Aichour, A., Zaghouane-Boudiaf, H., Mohamed Zuki, F.B., Kheireddine Aroua, M., Ibbora, C.V., 2019. Low-cost, biodegradable and highly effective adsorbents for batch and column fixed bed adsorption processes of methylene blue. J. Environ. Chem. Eng. 7, 103409 https://doi.org/10.1016/j.jece.2019.103409.

Albakri, M.A., Abdelnaby, M.M., Saleh, T.A., Al Hamouz, O.C.S., 2018. New series of benzene-1,3,5-triamine based cross-linked polyamines and polyamine/CNT composites for lead ion removal from aqueous solutions. Chem. Eng. J. 333, 76–84. https://doi.org/10.1016/j.cej.2017.09.152.

Albayati, T.M., Kalash, K.R., 2020. Polycyclic aromatic hydrocarbons adsorption from wastewater using different types of prepared mesoporous materials MCM-41in batch and fixed bed column. Process Saf. Environ. Prot. 133, 124–136. https://doi.org/10.1016/j.psep.2019.11.007.

Alijani, H., Shariatinia, Z., 2017. Effective aqueous arsenic removal using zero valent iron doped MWCNT synthesized by in situ CVD method using natural α-Fe2O3as a precursor. Chemosphere. https://doi.org/10.1016/j.chemosphere.2016.12.106.

Alkurdi, S.S.A., Al-Juboori, R.A., Bundschuh, J., Bowtell, L., Marchuk, A., 2021. Inorganic arsenic species removal from water using bone char: a detailed study on adsorption kinetic and isotherm models using error functions analysis. J. Hazard. Mater. 405, 124112 https://doi.org/10.1016/j.jhazmat.2020.124112.

Almomani, F., Bhosale, R., Khraisheh, M., Kumar, A., Almomani, T., 2020. Heavy metal ions removal from industrial wastewater using magnetic nanoparticles (MNP). Appl. Surf. Sci. 506, 144924 https://doi.org/10.1016/j.apsusc.2019.144924.

AlSalhi, M.S., Aziz, M.H., Atif, M., Fatima, M., Shaheen, F., Devanesan, S., Aslam Farooq, W., 2020. Synthesis of NiO nanoparticles and their evaluation for photodynamic therapy against HeLa cancer cells. J. King Saud. Univ. Sci. 32, 1395–1402. https://doi.org/10.1016/j.jksus.2019.11.033.

Ang, T.N., Young, B.R., Taylor, M., Burrell, R., Aroua, M.K., Baroutian, S., 2020. Breakthrough analysis of continuous fixed-bed adsorption of sevoflurane using activated carbons. Chemosphere 239, 124839. https://doi.org/10.1016/j.chemosphere.2019.124839.

Azam, K., Akhtar, S., Gong, Y.Y., Routledge, M.N., Ismail, A., Oliveira, C.A.F., Iqbal, S.Z., Ali, H., 2021. Evaluation of the impact of activated carbon-based filtration system on the concentration of aflatoxins and selected heavy metals in roasted coffee. Food Control 121, 107583. https://doi.org/10.1016/j.foodcont.2020.107583.

Bankole, M.T., Mohammed, I.A., Abdulkareem, A.S., Tijani, J.O., Ochigbo, S.S., Abubakre, O.K., Afolabi, A.S., 2018a. Optimization of supported bimetallic (Fe-Co/CaCO3) catalyst synthesis parameters for carbon nanotubes growth using factorial experimental design. J. Alloy. Compd. 749, 85–102. https://doi.org/10.1016/j.jallcom.2018.03.150.

Bhaumik, M., Maity, A., Brink, H.G., 2020. Zero valent nickel nanoparticles decorated polyaniline nanotubes for the efficient removal of Pb(II) from aqueous solution: synthesis, characterization and mechanism investigation. Chem. Eng. J., 127910 https://doi.org/10.1016/j.cej.2020.127910.

Bo, S., Luo, J., An, Q., Xiao, Z., Wang, H., Cai, W., Zhai, S., Li, Z., 2020. Efficiently selective adsorption of Pb(II) with functionalized alginate-based adsorbent in batch/column systems: mechanism and application simulation. J. Clean. Prod. 250, 119585 https://doi.org/10.1016/j.jclepro.2019.119585.

Bounab, N., Duclaux, L., Reinert, L., Oumedjbeur, A., Boukhalfa, C., Penhoud, P., Muller, F., 2021. Improvement of zero valent iron nanoparticles by ultrasound-assisted synthesis, study of Cr(VI) removal and application for the treatment of metal surface processing wastewater. J. Environ. Chem. Eng. 9. https://doi.org/10.1016/j.jece.2020.104773.

Cao, D.Q., Wang, X., Wang, Q.H., Fang, X.M., Jin, J.Y., Hao, X., Di, Iritani, E., Katagiri, N., 2020. Removal of heavy metal ions by ultrafiltration with recovery of extracellular polymer substances from excess sludge. J. Membr. Sci. 606, 118103 https://doi.org/10.1016/j.memsci.2020.118103.

Chen, Q., Yao, Y., Li, X., Lu, J., Zhou, J., Huang, Z., 2018. Comparison of heavy metal removals from aqueous solutions by chemical precipitation and characteristics of precipitates. J. Water Process Eng. 26, 289–300. https://doi.org/10.1016/j.jwpe.2018.11.003.

Chen, W.Q., Veksha, A., Lisak, G., 2020. Graphene-like carbon nanosheets grown over alkali-earth metal oxides: effects of chemical composition and physico-chemical properties. Carbon. https://doi.org/10.1016/j.carbon.2019.12.048.

Chowdhury, A., Kumari, S., Khan, A.A., Chandra, M.R., Hussain, S., 2021. Activated carbon loaded with Ni-Co-S nanoparticle for superior adsorption capacity of antibiotics and dye from wastewater: kinetics and isotherms. Colloids Surf. A Physicochem. Eng. Asp. 611, 125868 https://doi.org/10.1016/j.colsurfa.2020.125868.

Cristaldi, A., Conti, G.O., Jho, E.H., Zuccarello, P., Grasso, A., Copat, C., Ferrante, M., 2017. Phytoremediation of contaminated soils by heavy metals and PAHs. A brief review. Environ. Technol. Innov. 8, 309–326. https://doi.org/10.1016/j.eti.2017.08.002.

Ding, R., Lisak, G., 2019. Sponge-based microfluidic sampling for potentiometric ion sensing. Anal. Chim. Acta 1091, 103–111. https://doi.org/10.1016/j.aca.2019.09.024.

Ding, R., Krikstolaityte, V., Lisak, G., 2019. Inorganic salt modified paper substrates utilized in paper based microfluidic sampling for potentiometric determination of heavy metals. Sens. Actuators B Chem. 290, 347–356. https://doi.org/10.1016/j.snb.2019.03.079.

Ding, R., Cheong, Y.H., Ahamed, A., Lisak, G., 2021. Heavy metals detection with paper-based electrochemical sensors. Anal. Chem. 93, 1880–1888. https://doi.org/10.1021/acs.analchem.0c04247.

Doan, V.D., Phung, M.T., Nguyen, T.L.H., Mai, T.C., Nguyen, T.D., 2020. Noble metallic nanoparticles from waste Nypa fruticans fruit husk: biosynthesis, characterization, antibacterial activity and recyclable catalysis. Arab. J. Chem. 13, 7490–7503. https://doi.org/10.1016/j.arabjc.2020.08.024.

Egbosiuba, T.C., Abdulkareem, A.S., Kovo, A.S., Afolabi, E.A., Tijani, J.O., Roos, W.D., 2020. Enhanced adsorption of As(V) and Mn(VII) from industrial wastewater using multi-walled carbon nanotubes and carboxylated multi-walled carbon nanotubes. Chemosphere 254, 126780. https://doi.org/10.1016/j.chemosphere.2020.126780.

Egbosiuba, T.C., Abdulkareem, A.S., Kovo, A.S., Afolabi, E.A., Tijani, J.O., Bankole, M.T., Bo, S., Roos, W.D., 2021a. Adsorption of Cr(VI), Ni(II), Fe(II) and Cd(II) ions by KIAgNPs decorated MWCNTs in a batch and fixed bed process. Sci. Rep. 11, 1–20. https://doi.org/10.1038/s41598-020-79857-z.

Egbosiuba, T.C., Abdulkareem, A.S., Tijani, J.O., Ani, J.I., Krikstolaityte, V., Srinivasan, M., Veksha, A., Lisak, G., 2021b. Taguchi optimization design of diameter-controlled synthesis of multi walled carbon nanotubes for the adsorption of Pb(II) and Ni(II) from chemical industry wastewater. Chemosphere 266, 128937. https://doi.org/10.1016/j.chemosphere.2020.128937.

Fallah, N., Taghizadeh, M., 2020. Continuous fixed-bed adsorption of Mo(VI) from aqueous solutions by Mo(VI)-IIP: breakthrough curves analysis and mathematical modeling. J. Environ. Chem. Eng. 8, 104079 https://doi.org/10.1016/j.jece.2020.104079.

Franco, D.S.P., Fagundes, J.L.S., Georgin, J., Salau, N.P.G., Dotto, G.L., 2020. A mass transfer study considering intraparticle diffusion and axial dispersion for fixed-bed adsorption of crystal violet on pecan pericarp (Carya illinoensis). Chem. Eng. J. 397, 125423 https://doi.org/10.1016/j.cej.2020.125423.

de Franco, M.A.E., de Carvalho, C.B., Bonetto, M.M., de Pelegrini Soares, R., Féris, L.A., 2018. Diclofenac removal from water by adsorption using activated carbon in batch mode and fixed-bed column: isotherms, thermodynamic study and breakthrough curves modeling. J. Clean. Prod. 181, 145–154. https://doi.org/10.1016/j.jclepro.2018.01.138.

Ghasemi, S.S., Hadavifar, M., Maleki, B., Mohammadnia, E., 2019. Adsorption of mercury ions from synthetic aqueous solution using polydopamine decorated SWCNTs. J. Water Process Eng. 32, 100965 https://doi.org/10.1016/j.jwpe.2019.100965.

Gödde, J., Merko, M., Xia, W., Muhler, M., 2021. Nickel nanoparticles supported on nitrogen–doped carbon nanotubes are a highly active, selective and stable CO_2 methanation catalyst. J. Energy Chem. 54, 323–331. https://doi.org/10.1016/j.jechem.2020.06.007.

Govarthanan, M., Lee, S.M., Kamala-Kannan, S., Oh, B.T., 2015. Characterization, real-time quantification and in silico modeling of arsenate reductase (arsC) genes in arsenic-resistant Herbaspirillum sp. GW103. Res. Microbiol. 166, 196–204. https://doi.org/10.1016/j.resmic.2015.02.007.

Govarthanan, M., Mythili, R., Selvankumar, T., Kamala-Kannan, S., Kim, H., 2018. Myco-phytoremediation of arsenic- and lead-contaminated soils by Helianthus annuus and wood rot fungi, Trichoderma sp. isolated from decayed wood. Ecotoxicol. Environ. Saf. 151, 279–284. https://doi.org/10.1016/j.ecoenv.2018.01.020.

Gu, M., Hao, L., Wang, Y., Li, X., Chen, Y., Li, W., Jiang, L., 2020. The selective heavy metal ions adsorption of zinc oxide nanoparticles from dental wastewater. Chem. Phys. 534, 110750 https://doi.org/10.1016/j.chemphys.2020.110750.

Guo, X., Wang, J., 2019. A general kinetic model for adsorption: theoretical analysis and modeling. J. Mol. Liq. 288, 111100 https://doi.org/10.1016/j.molliq.2019.111100.

Gupta, A., Garg, A., 2019. Adsorption and oxidation of ciprofloxacin in a fixed bed column using activated sludge derived activated carbon. J. Environ. Manag. 250, 109474 https://doi.org/10.1016/j.jenvman.2019.109474.

Hang, Y., Si, Y., Zhou, Q., Yin, H., Wang, A., Cao, A., 2019. Morphology-controlled synthesis of calcium titanate particles and adsorption kinetics, isotherms, and thermodynamics of Cd(II), Pb(II), and Cu(II) cations. J. Hazard. Mater. 380, 120789 https://doi.org/10.1016/j.jhazmat.2019.120789.

Hayati, B., Maleki, A., Najafi, F., Gharibi, F., McKay, G., Gupta, V.K., Harikaranahalli Puttaiah, S., Marzban, N., 2018. Heavy metal adsorption using PAMAM/CNT nanocomposite from aqueous solution in batch and continuous fixed bed systems. Chem. Eng. J. 346, 258–270. https://doi.org/10.1016/j.cej.2018.03.172.

Hu, C., Le, A.T., Pung, S.Y., Stevens, L., Neate, N., Hou, X., Grant, D., Xu, F., 2021. Efficient dye-removal via Ni-decorated graphene oxide-carbon nanotube nanocomposites. Mater. Chem. Phys. 260, 124117 https://doi.org/10.1016/j.matchemphys.2020.124117.

Huang, X., Zhao, S., Abu-omar, M., Whelton, A.J., 2017. In-situ cleaning of heavy metal contaminated plastic water pipes using a biomass derived ligand. Biochem. Pharmacol. https://doi.org/10.1016/j.jece.2017.07.003.

Huang, X., Zemlyanov, D.Y., Diaz-Amaya, S., Salehi, M., Stanciu, L., Whelton, A.J., 2020. Competitive heavy metal adsorption onto new and aged polyethylene under various drinking water conditions. J. Hazard. Mater. 385, 121585 https://doi.org/10.1016/j.jhazmat.2019.121585.

Ibrahim, Y., Naddeo, V., Banat, F., Hasan, S.W., 2020. Preparation of novel polyvinylidene fluoride (PVDF)-Tin(IV) oxide (SnO2) ion exchange mixed matrix membranes for the removal of heavy metals from aqueous solutions. Sep. Purif. Technol. 250, 117250 https://doi.org/10.1016/j.seppur.2020.117250.

Ifthikar, J., Shahib, I.I., Sellaoui, L., Jawad, A., Zhao, M., Chen, Zhuqi, Chen, Zhulei, 2020. pH tunable anionic and cationic heavy metal reduction coupled adsorption by thiol cross-linked composite: physicochemical interpretations and fixed-bed column mathematical model study. Chem. Eng. J. 401, 126041 https://doi.org/10.1016/j.cej.2020.126041.

Jin, L., Zhao, X., Qian, X., Dong, M., 2018. Nickel nanoparticles encapsulated in porous carbon and carbon nanotube hybrids from bimetallic metal-organic-frameworks for highly efficient adsorption of dyes. J. Colloid Interface Sci. 509, 245–253. https://doi.org/10.1016/j.jcis.2017.09.002.

Joon, N.K., Ek, P., Zevenhoven, M., Hupa, L., Miró, M., Bobacka, J., Lisak, G., 2020. On-line microcolumn-based dynamic leaching method for investigation of lead bioaccessibility in shooting range soils. Chemosphere 256. https://doi.org/10.1016/j.chemosphere.2020.127022.

Jun, B.M., Kim, S., Kim, Y., Her, N., Heo, J., Han, J., Jang, M., Park, C.M., Yoon, Y., 2019. Comprehensive evaluation on removal of lead by graphene oxide and metal organic framework. Chemosphere 231, 82–92. https://doi.org/10.1016/j.chemosphere.2019.05.076.

Karpagavinayagam, P., Emi Princess Prasanna, A., Vedhi, C., 2020. Eco-friendly synthesis of nickel oxide nanoparticles using Avicennia marina leaf extract: morphological characterization and electrochemical application. Mater. Today Proc. https://doi.org/10.1016/j.matpr.2020.04.183.

Kharrazi, S.M., Mirghaffari, N., Dastgerdi, M.M., Soleimani, M., 2020. A novel post-modification of powdered activated carbon prepared from lignocellulosic waste through thermal tension treatment to enhance the porosity and heavy metals adsorption. Powder Technol. https://doi.org/10.1016/j.powtec.2020.01.065.

Lalhmunsiama, Pawar, R.R., Hong, S.M., Jin, K.J., Lee, S.M., 2017. Iron-oxide modified sericite alginate beads: a sustainable adsorbent for the removal of As(V) and Pb(II) from aqueous solutions. J. Mol. Liq. 240, 497–503. https://doi.org/10.1016/j.molliq.2017.05.086.

Lei, T., Li, S.J., Jiang, F., Ren, Z.X., Wang, L.L., Yang, X.J., Tang, L.H., Wang, S.X., 2019. Adsorption of cadmium ions from an aqueous solution on a highly stable dopamine-modified magnetic nano-adsorbent. Nanoscale Res. Lett. 14. https://doi.org/10.1186/s11671-019-3154-0.

Liu, D., Deng, S., Maimaiti, A., Wang, B., Huang, J., Wang, Y., Yu, G., 2018a. As(III) and As(V) adsorption on nanocomposite of hydrated zirconium oxide coated carbon nanotubes. J. Colloid Interface Sci. 511, 277–284. https://doi.org/10.1016/j.jcis.2017.10.004.

Liu, H., Xu, F., Xie, Y., Wang, C., Zhang, A., Li, L., Xu, H., 2018b. Effect of modified coconut shell biochar on availability of heavy metals and biochemical characteristics of soil in multiple heavy metals contaminated soil. Sci. Total Environ. 645, 702–709. https://doi.org/10.1016/j.scitotenv.2018.07.115.

Liu, Y., Gao, Q., Li, C., Liu, S., Xia, K., Han, B., Zhou, C., 2019. Effective coating of crosslinked polyethyleneimine on elastic spongy monolith for highly efficient batch and continuous flow adsorption of Pb(II) and acidic red 18. Chem. Eng. J., 123610 https://doi.org/10.1016/j.cej.2019.123610.

Liu, Y., Ji, D., Li, M., Xiao, J., Dong, P., Zhang, C., Han, L., Zhang, Y., 2020. Facile synthesis of cobalt nanoparticles encapsulated in nitrogen-doped carbon nanotubes for use as a highly efficient bifunctional catalyst in rechargeable Zn-air batteries. J. Alloy. Compd. 842, 155791 https://doi.org/10.1016/j.jallcom.2020.155791.

Liu, Z., Li, B., Shi, X., Li, L., Feng, Y., Jia, D., Zhou, Y., 2021. Target-oriented synthesis of high synthetic yield carbon dots with tailored surface functional groups for bioimaging of zebrafish, flocculation of heavy metal ions and ethanol detection. Appl. Surf. Sci. 538. https://doi.org/10.1016/j.apsusc.2020.148118.

Lung, I., Stan, M., Opris, O., Soran, M.L., Senila, M., Stefan, M., 2018. Removal of lead (II), cadmium(II), and arsenic(III) from aqueous solution using magnetite nanoparticles prepared by green synthesis with Box–Behnken design. Anal. Lett. 51, 2517–2529. https://doi.org/10.1080/00032719.2018.1446974.

Luo, M., Lin, H., He, Y., Li, B., Dong, Y., Wang, L., 2019. Efficient simultaneous removal of cadmium and arsenic in aqueous solution by titanium-modified ultrasonic biochar. Bioresour. Technol. 284, 333–339. https://doi.org/10.1016/j.biortech.2019.03.108.

Martinez–Vargas, S., Martínez, A.I., Hernández–Beteta, E.E., Mijangos–Ricardez, O.F., Vázquez–Hipólito, V., Patiño-Carachure, C., López–Luna, J., 2018. As(III) and As(V) adsorption on manganese ferrite nanoparticles. J. Mol. Struct. 1154, 524–534. https://doi.org/10.1016/j.molstruc.2017.10.076.

Maslova, M., Ivanenko, V., Yanicheva, N., Gerasimova, L., 2020. The effect of heavy metal ions hydration on their sorption by a mesoporous titanium phosphate ion-exchanger. J. Water Process Eng. 35, 101233 https://doi.org/10.1016/j.jwpe.2020.101233.

Min, K.J., Kim, J.H., Park, K.Y., 2021. Characteristics of heavy metal separation and determination of limiting current density in a pilot-scale electrodialysis process for plating wastewater treatment. Sci. Total Environ. 757, 143762 https://doi.org/10.1016/j.scitotenv.2020.143762.

Mohammadreza, B., Hossein, A., Mohammad, E., Ali, E., Alireza, B., 2021. Comprehensive batch and continuous methyl orange removal studies using surfactant modified chitosan-clinoptilolite composite. Sep. Purif. Technol.

Moo, J.G.S., Veksha, A., Da Oh, W., Giannis, A., Udayanga, W.D.C., Lin, S.X., Ge, L., Lisak, G., 2019. Plastic derived carbon nanotubes for electrocatalytic oxygen reduction reaction: effects of plastic feedstock and synthesis temperature. Electrochem. Commun. 101, 11–18. https://doi.org/10.1016/j.elecom.2019.02.014.

Naseem, T., Durrani, T., 2021. The role of some important metal oxide nanoparticles for wastewater and antibacterial applications: a review. Environ. Chem. Ecotoxicol. 3, 59–75. https://doi.org/10.1016/j.enceco.2020.12.001.

Nasir, A.M., Goh, P.S., Ismail, A.F., 2019. Highly adsorptive polysulfone/hydrous iron-nickel-manganese (PSF/HINM) nanocomposite hollow fiber membrane for synergistic arsenic removal. Sep. Purif. Technol. 213, 162–175. https://doi.org/10.1016/j.seppur.2018.12.040.

Pawar, R.R., Kim, M., Kim, J., Hong, S., Sawant, S.Y., Mok, S., 2018. Efficient removal of hazardous lead, cadmium, and arsenic from aqueous environment by iron oxide modified clay-activated carbon composite beads. Appl. Clay Sci. 162, 339–350. https://doi.org/10.1016/j.clay.2018.06.014.

Pelalak, R., Heidari, Z., Khatami, S.M., Kurniawan, T.A., Marjani, A., Shirazian, S., 2021. Oak wood ash/GO/Fe3O4 adsorption efficiencies for cadmium and lead removal from aqueous solution: kinetics, equilibrium and thermodynamic evaluation. Arab. J. Chem. 14, 102991 https://doi.org/10.1016/j.arabjc.2021.102991.

Prakash, A.A., Rajasekar, A., Sarankumar, R.K., AlSalhi, M.S., Devanesan, S., Aljaafreh, M.J., Govarthanan, M., Sayed, S.R.M., 2021. Metagenomic analysis of microbial community and its role in bioelectrokinetic remediation of tannery contaminated soil. J. Hazard. Mater. 412, 125133 https://doi.org/10.1016/j.jhazmat.2021.125133.

Prayoonpunratn, P., Jedsukontorn, T., Hunsom, M., 2020. Photocatalytic activity of metal nanoparticle-decorated titanium dioxide for simultaneous H2 production and biodiesel wastewater remediation. Chin. J. Chem. Eng. https://doi.org/10.1016/j.cjche.2020.08.010.

Qu, J., Tian, X., Jiang, Z., Cao, B., Akindolie, M.S., Hu, Q., Feng, C., Feng, Y., Meng, X., Zhang, Y., 2020. Multi-component adsorption of Pb(II), Cd(II) and Ni(II) onto microwave-functionalized cellulose: kinetics, isotherms, thermodynamics, mechanisms and application for electroplating wastewater purification. J. Hazard. Mater. 387. https://doi.org/10.1016/j.jhazmat.2019.121718.

Rocha, L.S., Almeida, Â., Nunes, C., Henriques, B., Coimbra, M.A., Lopes, C.B., Silva, C. M., Duarte, A.C., Pereira, E., 2016. Simple and effective chitosan based films for the removal of Hg from waters: equilibrium, kinetic and ionic competition. Chem. Eng. J. 300, 217–229. https://doi.org/10.1016/j.cej.2016.04.054.

Saravanan, A., Kumar, P.S., Govarthanan, M., George, C.S., Vaishnavi, S., Moulishwaran, B., Kumar, S.P., Jeevanantham, S., Yaashikaa, P.R., 2021. Adsorption characteristics of magnetic nanoparticles coated mixed fungal biomass for toxic Cr (VI) ions in aquatic environment. Chemosphere 267, 129226. https://doi.org/10.1016/j.chemosphere.2020.129226.

Shim, J., Kumar, M., Mukherjee, S., Goswami, R., 2019. Sustainable removal of pernicious arsenic and cadmium by a novel composite of MnO2 impregnated alginate beads: a cost-effective approach for wastewater treatment. J. Environ. Manag. 234, 8–20. https://doi.org/10.1016/j.jenvman.2018.12.084.

Singh, A., Kumar, D., Gaur, J.P., 2012. Continuous metal removal from solution and industrial effluents using Spirogyra biomass-packed column reactor. Water Res. 46, 779–788. https://doi.org/10.1016/j.watres.2011.11.050.

Vaneeckhaute, C., Darveau, O., Meers, E., 2019. Fate of micronutrients and heavy metals in digestate processing using vibrating reversed osmosis as resource recovery technology. Sep. Purif. Technol. 223, 81–87. https://doi.org/10.1016/j.seppur.2019.04.055.

Veksha, A., Yin, K., Moo, J.G.S., Da Oh, W., Ahamed, A., Chen, W.Q., Weerachanchai, P., Giannis, A., Lisak, G., 2020. Processing of flexible plastic packaging waste into pyrolysis oil and multi-walled carbon nanotubes for electrocatalytic oxygen reduction. J. Hazard. Mater. 387, 121256 https://doi.org/10.1016/j.jhazmat.2019.121256.

Wang, J., Guo, X., 2020. Adsorption kinetic models: physical meanings, applications, and solving methods. J. Hazard. Mater. 390, 122156 https://doi.org/10.1016/j.jhazmat.2020.122156.

WHO, 2017. Guidelines for Drinking-Water Quality, Fourth ed., p. 631. https://doi.org/10.1016/S1462-0758(00)00006-6

Winiarski, J.P., Rampanelli, R., Bassani, J.C., Mezalira, D.Z., Jost, C.L., 2020. Multi-walled carbon nanotubes/nickel hydroxide composite applied as electrochemical sensor for folic acid (vitamin B9) in food samples. J. Food Compos. Anal. 92. https://doi.org/10.1016/j.jfca.2020.103511.

Wu, L.K., Wu, H., Zhang, H., Bin, Cao, H.Z., Hou, G.Y., Tang, Y.P., Zheng, G.Q., 2018. Graphene oxide/CuFe2O4 foam as an efficient absorbent for arsenic removal from water. Chem. Eng. J. 334, 1808–1819. https://doi.org/10.1016/j.cej.2017.11.096.

Yahya, M.D., Abubakar, H., Obayomi, K.S., Iyaka, Y.A., Suleiman, B., 2020. Simultaneous and continuous biosorption of Cr and Cu (II) ions from industrial tannery effluent using almond shell in a fixed bed column. Results Eng. 6, 100113 https://doi.org/10.1016/j.rineng.2020.100113.

Yang, Y., Zhang, H., Yan, Y., 2019. Synthesis of CNTs on stainless steel microfibrous composite by CVD: effect of synthesis condition on carbon nanotube growth and structure. Compos. Part B Eng. 160, 369–383. https://doi.org/10.1016/j.compositesb.2018.12.100.

Yatom, S., Selinsky, R.S., Koel, B.E., Raitses, Y., 2017. “Synthesis-on” and “synthesis-off” modes of carbon arc operation during synthesis of carbon nanotubes. Carbon 125, 336–343. https://doi.org/10.1016/j.carbon.2017.09.034 (N.Y.).

Yoo, J.C., Lee, C., Lee, J.S., Baek, K., 2017. Simultaneous application of chemical oxidation and extraction processes is effective at remediating soil co-contaminated with petroleum and heavy metals. J. Environ. Manag. 186, 314–319. https://doi.org/10.1016/j.jenvman.2016.03.016.

Zaidi, R., Khan, S.U., Azam, A., Farooqi, I.H., 2021. A study on effective adsorption of lead from an aqueous solution using copper oxide nanoparticles. IOP Conf. Ser. Mater. Sci. Eng. 1058, 012074 https://doi.org/10.1088/1757-899x/1058/1/012074.

Zhang, D., Zhang, K., Hu, X., He, Q., Yan, J., Xue, Y., 2021a. Cadmium removal by MgCl2 modified biochar derived from crayfish shell waste: batch adsorption, response surface analysis and fixed bed filtration. J. Hazard. Mater. 408, 124860 https://doi.org/10.1016/j.jhazmat.2020.124860.

Zhang, Q., Kazim, F.M., Ma, S., Qu, K., Li, M., Wang, Y., Hu, H., Cai, W., Yang, Z., 2021b. Nitrogen dopants in nickel nanoparticles embedded carbon nanotubes promote overall urea oxidation. Appl. Catal. B Environ. 280, 119436 https://doi.org/10.1016/j.apcatb.2020.119436.

Zhang, H., Xu, F., Xue, J., Chen, S., Wang, J., Yang, Y., 2020a. Enhanced removal of heavy metal ions from aqueous solution using manganese dioxide-loaded biochar: behavior and mechanism. Sci. Rep. 10, 1–13. https://doi.org/10.1038/s41598-020-63000-z.

Zhang, L., Niu, W., Sun, J., Zhou, Q., 2020b. Efficient removal of Cr(VI) from water by the uniform fiber ball loaded with polypyrrole: static adsorption, dynamic adsorption and mechanism studies. Chemosphere 248, 126102. https://doi.org/10.1016/j.chemosphere.2020.126102.

Zhang, Q., Ye, X., Li, H., Chen, D., Xiao, W., Zhao, S., Xiong, R., Li, J., 2020c. Cumulative effects of pyrolysis temperature and process on properties, chemical speciation, and environmental risks of heavy metals in magnetic biochar derived from coagulation-flocculation sludge of swine wastewater. J. Environ. Chem. Eng. 8, 104472 https://doi.org/10.1016/j.jece.2020.104472.

Zhang, Y., Wang, Y., Zhang, H., Li, Y., Zhang, Z., Zhang, W., 2020d. Recycling spent lithium-ion battery as adsorbents to remove aqueous heavy metals: adsorption kinetics, isotherms, and regeneration assessment. Resour. Conserv. Recycl. 156, 104688 https://doi.org/10.1016/j.resconrec.2020.104688.

Zhao, M., Huang, Z., Wang, S., Zhang, L., 2020. Ultrahigh efficient and selective adsorption of Au(III) from water by novel chitosan-coated MoS2 biosorbents: performance and mechanisms. Chem. Eng. J. 401, 126006 https://doi.org/10.1016/j.cej.2020.126006.

Zhao, W., Tian, Y., Chu, X., Cui, L., Zhang, H., Li, M., Zhao, P., 2021. Preparation and characteristics of a magnetic carbon nanotube adsorbent: its efficient adsorption and recoverable performances. Sep. Purif. Technol. 257, 117917 https://doi.org/10.1016/j.seppur.2020.117917.